ELSEVIER

Biophysical Chemistry 105 (2003) 293–322

Biophysical Chemistry

www.elsevier.com/locate/bpc

Chirality-dependent interactions between molecular propeller structures in solution. Chiral recognition and discrimination processes modulated by temperature and incremental changes in structural chirality

James P. Bolender[1], F.S. Richardson*

Department of Chemistry, University of Virginia, P.O. Box 400319, Charlottesville, VA 22904, USA

Received 9 October 2002; accepted 1 November 2002

Abstract

Time-resolved chiroptical luminescence (TR-CL) measurements are used to study chirality-dependent intermolecular interactions in dynamic excited-state quenching processes. The measurements are carried out on solution samples that contain a racemic mixture of chiral luminophore molecules (with enantiomeric structures denoted by ΛL and ΔL) and a small, optically resolved concentration of chiral quencher (CQ) molecules. The luminophores are excited with a pulse of linearly polarized laser radiation to produce an initially racemic excited-state population of ΛL^* and ΔL^* enantiomers, and TR-CL measurements are then used to monitor the differential decay kinetics of the ΛL^* and ΔL^* subpopulations. Observed differences between the ΛL^* and ΔL^* decay kinetics reflect differential rate processes and efficiencies for ΛL^*–CQ vs. ΔL^*–CQ quenching actions, and they are diagnostic of chiral discriminatory interactions between the luminophore and quencher molecules. Twelve different luminophore–quencher systems are examined, in both H_2O and D_2O solutions, and in each case the quenching kinetics are measured over the 273–308 K temperature range. In all of the systems examined here, quenching occurs via electronic energy-transfer processes in *transient* (ΛL^*–CQ) and (ΔL^*–CQ) encounter complexes, and the chiral discriminatory rate parameters reflect the relative stabilities and lifetimes of these complexes as well as their structures and internal (electronic and nuclear) dynamics. All of the luminophore and quencher molecules examined in this study have three-bladed propeller-like structures that are very similar in overall shape and size. However, they exhibit small differences in the structural details of their propeller blades, and it is found that these small differences in structure can produce both qualitative and very substantial quantitative differences in their chiral recognition and discrimination properties.
© 2003 Elsevier Science B.V. All rights reserved.

Keywords: Intermolecular chiral recognition; Chiral discrimination; Chiroptical luminescence spectroscopy; Excited-state quenching; Electronic energy transfer

*Corresponding author. Tel.: +1-434-924-3905; fax: +1-434-924-3966.
E-mail address: fsr@virginia.edu (F.S. Richardson).
[1] Present address: Department of Chemistry, University of San Diego, San Diego, CA 92110-2492, USA.

0301-4622/03/$ - see front matter © 2003 Elsevier Science B.V. All rights reserved.
doi:10.1016/S0301-4622(03)00081-4

1. Introduction

Intermolecular recognition and discrimination processes are of widespread interest and profound importance in chemistry and biology [1–6]. In systems that contain chiral molecular species, these processes are often governed by intermolecular interactions that depend on the relative structural chiralities of the interacting species. Considerable attention has been given to experimental characterization and theoretical rationalization of chirality-dependent molecular recognition/discrimination phenomena, but efforts to join theory with experimental observation have met with only mixed success. This is due, at least in part, to the difficulties involved in identifying and separately evaluating contributions made by the various *kinds* of structural chirality (electronic *and* stereochemical) typically found in chiral molecular systems. Furthermore, in most systems and processes of practical interest, chiral discriminatory interactions represent only a small fraction of the total intermolecular interaction energy, multiple interaction mechanisms are likely to make important contributions, and environmental effects can be substantial. In systems where the interacting molecules have highly differentiated stereochemical structures, it is sometimes possible to rationalize chiral discriminatory behavior in terms of steric/electrostatic 'lock-and-key' models. However, these models are of little value for treating systems in which the interacting molecules have *similar* shapes, sizes, and static charge distributions, and they do not address contributions to chiral discrimination from *dynamic electronic interactions* of the kinds found, for example, in intermolecular electronic energy-transfer processes and stereoselective electron-transfer reactions.

In the present study, we examine intermolecular chiral discrimination in dynamic excited-state quenching processes. We focus on a series of systems that contain a racemic mixture of chiral luminophores (with enantiomeric structures denoted here by ΛL and ΔL) in solution with a small, optically-resolved concentration of chiral quencher (CQ) species [7–17]. The luminophores are excited with a pulse of *unpolarized* light to produce an initially *racemic* excited-state population (of ΛL^* and ΔL^* enantiomers) that may subsequently evolve to a *non-racemic* composition in the presence of enantiopreferential quenching actions by the CQ species. The time-evolution of enantiomeric excess in the luminophore excited-state population is monitored by time-resolved chiroptical luminescence (TR-CL) measurements, and these measurements also yield rate constants for the competing ΛL^*–CQ and ΔL^*–CQ quenching processes. A comparison of these quenching rate constants (denoted here by k_q^{Λ} and k_q^{Δ}) provides information about both the degree and sense (handedness) of chiral discriminatory interactions between the luminophores (ΛL^* and ΔL^*) and the CQ species.

The luminophore and quencher molecules examined in this study are very similar in overall shape and size, but they differ in their chemical compositions, electronic state structures, and stereochemical details. Both the luminophores and quenchers have three-bladed propeller-like structures of well-defined helicity about either an exact or an approximate threefold symmetry axis. However, whereas the individual propeller blades of the luminophore structures are achiral and essentially flat, the individual propeller blades of the quencher structures are inherently chiral and contain several stereogenic atomic centers of well-defined absolute configuration. The chirality of the luminophore structures derives entirely from the helical arrangement of the propeller blades about the trigonal symmetry axis of these structures. In contrast, the overall chirality of the quencher systems reflects chiral structural details within each of the three propeller blades, as well as the overall helical arrangement of these blades about the propeller screw axis. Each of the several types of structural chirality present in the quencher systems may be expected to make distinct contributions to both the degree and sense of chiral recognition and discrimination observed in the luminophore–quencher interaction processes examined in this study. One of the major objectives of this study was to determine which elements of structural chirality in the quencher systems play the dominant role in the observed chiral recognition and discrimination phenomena. Does helicity about the screw axis of the overall, three-bladed propeller structures play the dominant

role, or do conformational helicities and local site asymmetries *within* the individual propeller blades of the structures play the dominant role?

The luminophores used in this study are tris(dipicolinate) coordination complexes of either Eu(III) or Tb(III). These complexes have tris-terdentate chelate structures of trigonal–dihedral (D_3) symmetry, and in aqueous solution they exist as a racemic mixture of interconverting structural enantiomers, denoted here by Λ-Ln(dpa)$_3^{3-}$ and Δ-Ln(dpa)$_3^{3-}$ (where Ln≡Eu^{3+} or Tb^{3+}; dpa≡dipicolinate dianion≡2,6-pyridinedicarboxylate; and Λ and Δ are chirality labels that specify either left-handed (Λ) or right-handed (Δ) structural helicity about the trigonal symmetry axis of the complexes). The electronic state structures relevant to the luminescence properties of these complexes have been studied in some detail and are reasonably well characterized [18,19]. In the Eu(dpa)$_3^{3-}$ complexes, the relevant state structure is that derived from the ^7F_J ($J=0$–6) and lowest-energy $^5D_0$ multiplet manifolds of the $4f^6(Eu^{3+})$ electronic configuration, and in the Tb(dpa)$_3^{3-}$ complexes the relevant state structure is that derived from the ^7F_J ($J=0$–6) and lowest-energy $^5D_4$ multiplet manifolds of the $4f^8(Tb^{3+})$ electronic configuration.

All of the quencher systems used in this study are six-coordinate Co(III) complexes constructed from *trans*-1,2-diaminocyclohexane ligands. Each of these complexes contains a $[CoN_6]^{3+}$ coordination core in which the nitrogen donor atoms are from ligand amino groups, and each contains chelate rings that have conformational chirality dictated by the absolute configuration (*R* or *S*) of the two stereogenic carbon atoms in each *trans*-1,2-diaminocyclohexane ligand. Four of the complexes have tris-bidentate chelate structures with ligand compositions specified by [Co(*R*,*R*-dach)$_{3-y}$(*S*,*S*-dach)$_y$]$^{3+}$ ($y=0$, 1, 2, or 3), where *R*,*R*-dach and *S*,*S*-dach denote, respectively, the 1(*R*),2(*R*) and 1(*S*),2(*S*) optical isomers of *trans*-1,2-diaminocyclohexane. The two remaining complexes employed as quenchers are derivatives of [Co(*R*,*R*-dach)$_3$]$^{3+}$ in which either one or both of the trigonal faces of the [Co(*R*,*R*-dach)$_3$]$^{3+}$ parent complex are capped by a tris(methylene)amino group attached to three nitrogen atoms of the $[CoN_6]^{3+}$ coordination core. These complexes contain either three or six additional stereogenic centers, located at the nitrogen atoms attached to the capping group (or groups).

Each of the [Co(*R*,*R*-dach)$_{3-y}$(*S*,*S*-dach)$_y$]$^{3+}$ complexes has a three-bladed propeller-like structure in which the screw axis of the propeller is coincident with either an exact or an approximate threefold symmetry axis of the complex. The main structural differences between these complexes are found in the shapes of the individual propeller blades (which reflect differences between the chelate-ring conformations dictated by *R*,*R*-dach vs. *S*,*S*-dach ligands) and in the orientational distributions of the six N–H bonds that protrude out from each trigonal face of the complexes. The orientations of the N–H bonds on the trigonal faces of these complexes may be expected to have a significant influence on any hydrogen-bonding interactions that might occur between the quencher complexes and the Ln(dpa)$_3^{3-}$ luminophores (which have carboxylate groups on their trigonal faces). Of course, these types of interactions would be in large part suppressed in systems where the *mono-capped* or *bi-capped* derivatives of [Co(*R*,*R*-dach)$_3$]$^{3+}$ are used as quenchers.

The excited-state quenching processes examined in this study occur via electronic energy transfer between excited Eu(dpa)$_3^{3-}$ or Tb(dpa)$_3^{3-}$ luminophores and ground-state Co(III) complexes. The energy donor levels of the excited luminophores (Eu* or Tb*) are in all cases at energies $<21\,500$ cm^{-1} (above ground), and they correspond to excited states formed by 4f–4f electronic excitations localized on the metal centers (Eu^{3+} or Tb^{3+}) of the luminophores. In all of the Co(III) complexes used in this study, the relevant energy acceptor levels correspond to states derived in large part from the $3d^6$ electronic configuration of Co^{3+}. Therefore, the resonant donor (deexcitation)–acceptor(excitation) transitions that occur in the Ln* + Co → Ln + Co* energy-transfer processes (where Ln*≡Eu* or Tb*) involve 4f–4f transitions in Ln* and 3d–3d transitions on Co. Both of these transition types have transition densities localized largely on the metal centers of the interacting luminophore and quencher molecules, and both exhibit relatively small oscillator strengths

(in optical absorption and/or emission processes). Given these properties of the donor (4f–4f) and acceptor (3d–3d) transition types, one may predict that energy transfer will occur predominantly via short-range interactions in transient Ln*–Co contact (or near-contact) pairs formed during diffusional encounters between the luminophores and quencher species in solution.

All of the measurements reported in this study were carried out on either H_2O or D_2O solution samples in which the luminophore concentration was 10 mM and the quencher concentration was 10 μM. Measurements were performed at eight different sample temperatures between 273 and 308 K, and the results obtained from these measurements reveal significant, thermally-induced modulations in the chirality-dependent quenching kinetics observed for the various luminophore–quencher systems. Moreover, the degrees of chiral recognition and discrimination observed in the quenching processes show a dependence on the electronic state structures, as well as the stereochemical structures, of the interacting luminophore and quencher molecules.

2. Elements of structural chirality in the luminophore and quencher molecules

2.1. $Eu(dpa)_3^{3-}$ and $Tb(dpa)_3^{3-}$ luminophores

The equilibrium structures of $Eu(dpa)_3^{3-}$ and $Tb(dpa)_3^{3-}$ in neutral aqueous solution have trigonal–dihedral (D_3) symmetry, and the three bicyclic chelate rings in these structures form either a *left-handed* (Λ) or a *right-handed* (Δ) three-bladed propeller arrangement about the threefold axis. The individual ligands and their chelate rings have *achiral* structures, so structural chirality in $Eu(dpa)_3^{3-}$ and $Tb(dpa)_3^{3-}$ complexes is determined entirely by the helical (propeller-like) distribution of chelate rings about the metal atom. Following standard practice, we label the structural enantiomers of these complexes as either Λ or Δ, which refer to the helicity of the three bicyclic chelate rings about the trigonal axis [20–22]. It is important to note, however, that although the Λ enantiomer is defined to have *left-handed* chirality about its trigonal (C_3) symmetry axis, it has *right-handed* chirality about each of its three digonal (C_2) symmetry axes. Analogously, the Δ enantiomer, defined to have *right-handed* chirality about its trigonal axis, has *left-handed* chirality about each of its digonal axes. The absolute configuration of a given enantiomer is uniquely specified by the label Λ or Δ, but to specify the 'handedness' of its structure one must also choose a particular reference axis. The chiroptical properties of this enantiomer are determined by its absolute configuration, irrespective of how one chooses to define its structural handedness. However, when considering interactions between this enantiomer and other chiral molecules, it is often useful (and sometimes essential) to specify the handedness of the enantiomer with respect to axes that are coincident with likely intermolecular interaction axes. Structural representations of Λ-$Ln(dpa)_3^{3-}$ and Δ-$Ln(dpa)_3^{3-}$ enantiomers are shown in Fig. 1, with views along both the trigonal axis and one of the digonal (C_2) axes.

Under the solution conditions employed in the present study, the $Eu(dpa)_3^{3-}$ and $Tb(dpa)_3^{3-}$ complexes exist as racemic mixtures in which the Λ an Δ enantiomers undergo relatively facile *intramolecular* $\Lambda \Leftrightarrow \Delta$ isomerization processes. The kinetics of these processes have been characterized for $Eu(dpa)_3^{3-}$ in both H_2O and D_2O solutions over the 293–353 K temperature range, and fits of the rate-constant data to Arrhenius and Eyring thermal activation models yield the parameters shown in Table 1 [23]. For $Eu(dpa)_3^{3-}$ in H_2O, the enantiomer interconversion rate constant increases from a value of 12 s^{-1} at 293 K to a value of 592 s^{-1} at 353 K, and for $Eu(dpa)_3^{3-}$ in D_2O, the rate constant increases from a value 6 s^{-1} at 293 K to a value of 371 s^{-1} at 353 K. Rate parameters for $Tb(dpa)_3^{3-}$ enantiomer-interconversion processes have not been determined, but they are expected to be closely similar to those determined for $Eu(dpa)_3^{3-}$ [11].

2.2. Quenchers

All of the cobalt(III) complexes examined as quenchers in this study have an octahedral $[CoN_6]^{3+}$ coordination core in which the nitrogen donor atoms are from ligand amino groups. The

building-block ligands are the 1(*R*),2(*R*) and 1(*S*),2(*S*) optical isomers of *trans*-1,2-diaminocyclohexane, which are denoted hereafter as *R,R*-dach and *S,S*-dach. Four of the complexes have tris-bidentate chelate structures, with ligand compositions specified by $[Co(R,R\text{-dach})_{3-y}(S,S\text{-dach})_y]^{3+}$ ($y=0$, 1, 2 or 3). The chelate rings in these structures form a three-bladed propeller with either a *left-handed* (Λ) or *right-handed* (Δ) screw sense, and the handedness of this propeller defines what is commonly called the *configurational chirality* of the overall chelate system. The Λ and Δ configurational isomers of the $[Co(R,R\text{-dach})_{3-y}(S,S\text{-dach})_y]^{3+}$ complexes may be resolved to obtain four diastereomeric structures with Λ configurational chirality and four with Δ configurational chirality. Only Δ-$[Co(R,R\text{-dach})_{3-y}(S,S\text{-dach})_y]^{3+}$ configurational isomers

Table 1
Thermal activation parameters determined for $\Lambda-Eu(dpa)_3^{3-} \rightleftarrows \Delta-Eu(dpa)_3^{3-}$ enantiomer interconversion kinetics in H_2O and D_2O solutions[a]

Parameter	Solvent	
	H_2O	D_2O
E_a (kJ mol^{-1})[b]	51.3	50.7
$\ln A$ (s^{-1})[b]	23.8	23.4
$\Delta H^{\ddagger}$ (kJ mol^{-1})[c]	48.6	48.0
$\Delta S^{\ddagger}$ (J mol^{-1} K^{-1})[c]	−55.8	−59.3

[a] Data from [23].
[b] Parameters determined from fits of enantiomer interconversion rate-constant data, $k_c(T)$, to $\ln k_c = \ln A - E_a/RT$.
[c] Parameters determined from fits of enantiomer interconversion rate-constant data, $k_c(T)$, to $\ln(k_c/T) = \ln(k_B/h) + \Delta S^{\ddagger}/R - \Delta H^{\ddagger}/RT$.

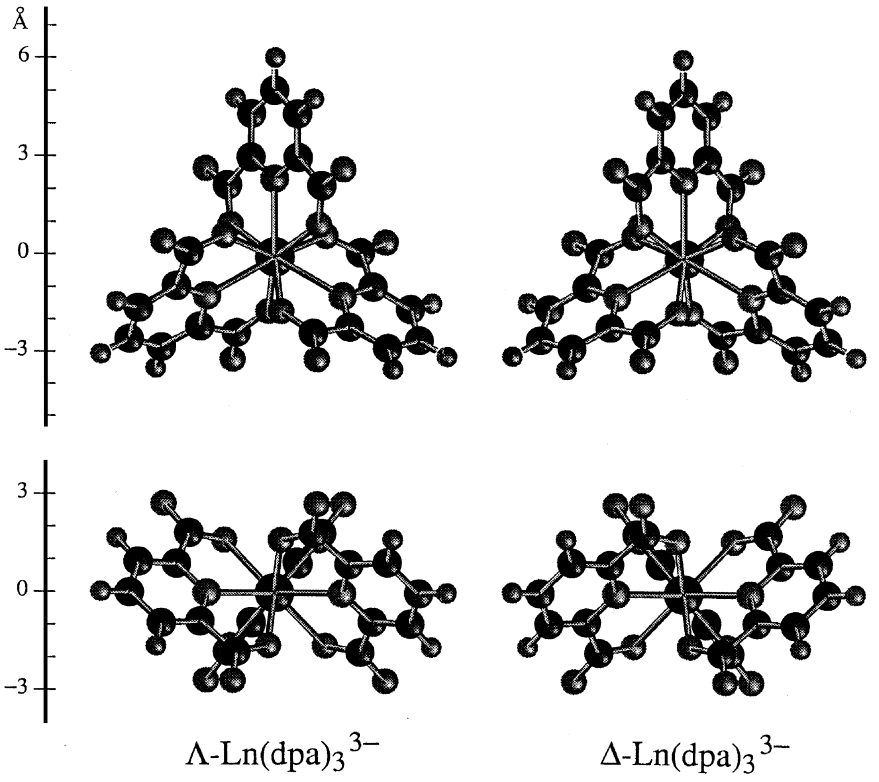

Fig. 1. Structural representations of Λ-$Ln(dpa)_3^{3-}$ and Δ-$Ln(dpa)_3^{3-}$ enantiomers. The top structures are viewed along the trigonal symmetry axis, and the bottom structures are viewed along one of the digonal (C_2) symmetry axes. The dimensions of the structures are indicated by the angstrom (Å) scales shown on the left-hand side of the figure.

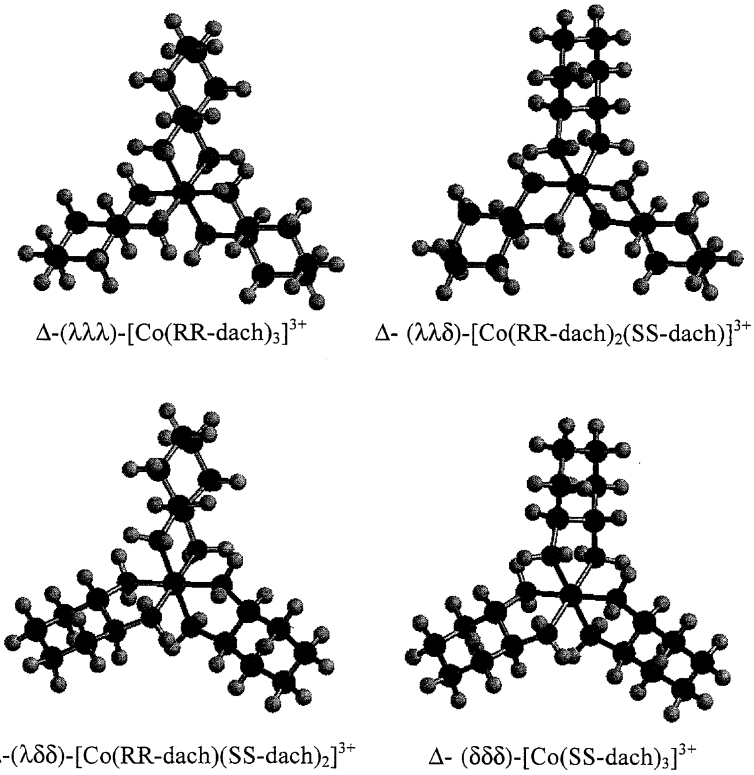

Fig. 2. Structural representations of the Δ configurational isomers of the $[Co(R,R\text{-dach})_{3-y}(S,S\text{-dach})_y]^{3+}$ ($y=0$, 1, 2, or 3) complexes, each viewed along the screw axis of the three-bladed propeller formed by the chelate rings.

are used in the present study. Each of these isomers has an enantiomeric counterpart among the Λ isomers.

The five-membered chelate rings formed by coordination of *trans*-1,2-dach to a Co^{3+} ion have rigid, non-planar conformational structures that are chiral. Chelate rings formed by *R,R*-dach have a *conformational chirality* opposite (in handedness) to that found in chelate rings formed by *S,S*-dach. Following conventions described elsewhere, the conformational chirality of *R,R*-dach chelate rings is designated as λ (referring to *left-handed* helicity about a particular reference axis), and the conformational chirality of *S,S*-dach chelate rings is designated as δ (referring to *right-handed* helicity about the same reference axis) [20–22]. Given these designations, the mixtures of chelate ring conformational chiralities in our four Δ-$[Co(R,R\text{-dach})_{3-y}(S,S\text{-dach})_y]^{3+}$ complexes are (λλλ), (λλδ), (λδδ) and (δδδ) for $y=0$, 1, 2 and 3, respectively. The following notation may now be used to give complete information about the types of structural chirality found in each complex: Δ-(λλλ)-$[Co(R,R\text{-dach})_3]^{3+}$; Δ-(λλδ)-$[Co(R,R\text{-dach})_2(S,S\text{-dach})]^{3+}$; Δ-(λδδ)-$[Co(R,R\text{-dach})(S,S\text{-dach})_2]^{3+}$; and Δ-(δδδ)-$[Co(S,S\text{-dach})_3]^{3+}$. However, since chelate-ring conformational chirality (λ or δ) is determined entirely by ligand chirality (*R,R* or *S,S*), information about the latter is contained in the λ/δ notation, and hereafter we shall use the following abbreviated notation to distinguish between the four complexes: Δ-(λλλ); Δ-(λλδ); Δ-(λδδ); and Δ-(δδδ). Structural representations of these complexes are shown in Fig. 2, with views *along* the screw axis of the three-bladed propeller formed by the chelate rings. Note that the Δ-(λλλ) and Δ-(δδδ) complexes each have D_3 point-group symmetry, with a threefold

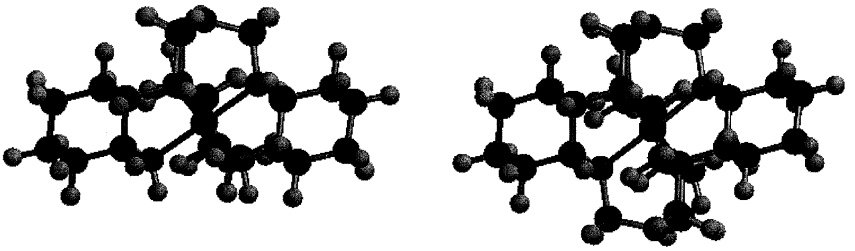

Δ-(λλλ)-mc Δ-(λλλ)-bc

Fig. 3. Structural representations of the *mono-capped* (*mc*) and *bi-capped* (*bc*) derivatives of Δ-(λλλ)-[Co(*R*,*R*-dach)$_3$]$^{3+}$, each viewed along a direction perpendicular to the threefold symmetry axis of the complex.

symmetry axis coincident with the propeller screw axis. The Δ-(λλδ) and Δ-(λδδ) complexes each have C_2 point-group symmetry, with a twofold axis that is perpendicular to the propeller screw axis.

Two additional cobalt(III) complexes were prepared and used as CQs in this study. One is a *mono-capped* and the other is a *bi-capped* derivative of Δ-(λλλ)-[Co(*R*,*R*-dach)$_3$]$^{3+}$ (≡Δ-(λλλ) in our abbreviated notation). In the mono-capped derivative, denoted here by Δ-(λλλ)-*mc*, one of the trigonal faces of the parent Δ-(λλλ) complex is capped by a tris(methylene)amino group attached to three nitrogen atoms of the $[CoN_6]^{3+}$ coordination core. In the bi-capped derivative, denoted here by Δ-(λλλ)-*bc*, *both* trigonal faces of the parent Δ-(λλλ) complex are capped by tris(methylene)amino groups. The Δ-(λλλ)-*mc* complex has C_3 point-group symmetry, and it contains *three* asymmetric N centers (each with *R* absolute configuration) in addition to the chiral structural elements found in the parent Δ-(λλλ) complex. The Δ-(λλλ)-*bc* complex has D_3 point-group symmetry, and it contains six asymmetric N centers (each with *R* absolute configuration) in addition to the chiral structural elements found in Δ-(λλλ). Structural representations of the Δ-(λλλ)-*mc* and Δ-(λλλ)-*bc* complexes are shown in Fig. 3.

All of the Co(III) complexes used as quenchers in this study have flattened spheroidal (oblate) shapes with equatorial radii of ≈6 Å and polar radii between 2.5 and 4 Å (the larger of the latter values applies to the bi-capped [Co(*R*,*R*-dach)$_3$]$^{3+}$ derivative). These general shapes and approximate sizes of the quencher species are very similar to the shapes and sizes of the Eu(dpa)$_3^{3-}$ and Tb(dpa)$_3^{3-}$ luminophores. The most interesting differences between the quencher structures (with respect to their relationship to enantiopreferential quenching rates and efficiencies) are: (1) the relative distributions of chelate-ring conformational isomers (λ vs. δ); (2) the relative availabilities and orientations of amino (donor group) N–H bonds for hydrogen-bonding interactions with luminophores; and, (3) the relative accessibility of the $[CoN_6]^{3+}$ coordination core to luminophores (in luminophore–quencher contact encounters).

3. Electronic state structures and optical properties of the luminophores and quenchers

3.1. Luminophores

The optical excitation and emission properties of Eu(dpa)$_3^{3-}$ and Tb(dpa)$_3^{3-}$ complexes have been studied extensively in both solid-state and solution-phase samples [18,19]. Analyses of these properties have produced reasonably good characterizations of the crystal-field energy-level structures within the ^7F_J (J=0–6) multiplet manifolds of both Eu^{3+} and Tb^{3+}, the lowest-energy $^5D_0$, $^5D_1$, $^5D_2$ multiplet manifolds of Eu^{3+}, and the lowest-energy $^5D_4$ multiplet manifold of Tb^{3+}. The locations and widths of these $4f^6(Eu^{3+})$ and $4f^8(Tb^{3+})$ multiplet manifolds are shown in the energy-level diagram of Fig. 4. For Eu(dpa)$_3^{3-}$ in

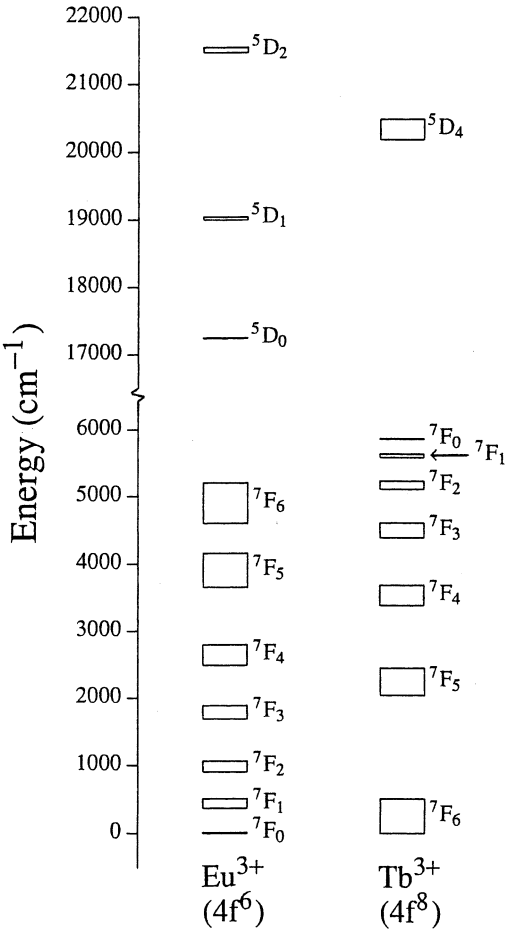

Fig. 4. Locations and widths of the ^7F_J and lowest-energy ^5D_J multiplet manifolds of $Eu^{3+}(4f^6)$ and $Tb^{3+}(4f^8)$ in $Eu(dpa)_3^{3-}$ and $Tb(dpa)_3^{3-}$ complexes. The widths of the respective manifolds reflect energy differences between the lowest and highest crystal-field levels split out of the parent $^{2S+1}L_J$ multiplet states.

solution, the emitting state is $^5D_0$, and the most intense luminescence is observed in the $^7F_2 \leftarrow {}^5D_0$ and $^7F_4 \leftarrow {}^5D_0$ transition regions. However, the luminescence observed in the $^7F_1 \leftarrow {}^5D_0$ transition region exhibits the strongest chiroptical properties, and most of the $Eu(dpa)_3^{3-}$ luminescence measurements reported in this paper were carried out at an emission wavelength that corresponds to one (of the two) crystal-field components of the $^7F_1 \leftarrow {}^5D_0$ transition. For $Tb(dpa)_3^{3-}$ in solution, emission occurs from crystal-field levels of the $^5D_4$ multiplet, and luminescence is observed in each of the seven ^7F_J $(J=0–6) \leftarrow {}^5D_4$ transition regions. The most intense luminescence is observed in the $^7F_5 \leftarrow {}^5D_4$ transition region, and this luminescence also exhibits strong chiroptical properties. Our TR-CL measurements on $Tb(dpa)_3^{3-}$ are carried out at emission wavelengths within the $^7F_5 \leftarrow {}^5D_4$ transition region.

3.2. Quenchers

In the present study, the relevant electronic (and vibronic) states of the quencher molecules are those that can provide acceptor levels for Eu*-to-Co and Tb*-to-Co energy-transfer processes (where Eu* and Tb* denote $Eu(dpa)_3^{3-}$ and $Tb(dpa)_3^{3-}$ complexes in their $^5D_0$ and $^5D_4$ excited states, respectively, and Co denotes a Co(III) quencher complex in its ground electronic state). The $^5D_0$ donor state of Eu* is located approximately 17190 cm^{-1} (above ground), and the $^5D_4$ donor levels of Tb* span the interval 20 450–20 505 cm^{-1} (above ground). The donor deexcitation pathways relevant to the Eu*-to-Co energy-transfer processes are through one or more of the seven $^7F_J \leftarrow {}^5D_0$ transition manifolds of Eu*, the lowest-energy of which spans the interval 12 030–12 250 cm^{-1} and the highest-energy of which is centered at 17 190 cm^{-1}. The donor deexcitation pathways relevant to the Tb*-to-Co energy-transfer processes are through one or more of the seven $^7F_J \leftarrow {}^5D_4$ transition manifolds of Tb*, the lowest- and highest-energy of which span the intervals 14 710–14 765 and 20 290–20 505 cm^{-1}, respectively. It follows that all of the Eu*(deexcitation)–Co(excitation) transition resonances germane to the energy-transfer processes examined in this study must be at energies between 12 030 and 17 190 cm^{-1}, and the Tb*(deexcitation)–Co(excitation) transition resonances must be at energies between 14 710 and 20 505 cm^{-1}. For each of the six Co(III) complexes used as quenchers in the present study, all of the transitions falling within these energy regions correspond to 3d–3d electronic (or vibronic) excitations localized within the $[CoN_6]^{3+}$ coordination core of the complexes.

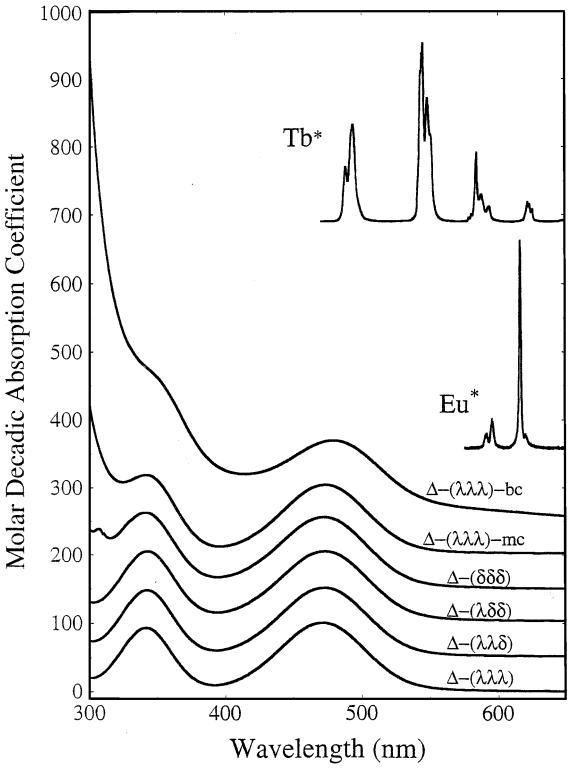

Fig. 5. Absorption spectra recorded over the 300–650 nm wavelength range for the six Co(III) complexes employed as quenchers in the present study. The inset spectra (shown in the upper part of the figure) display those parts of the $Tb(dpa)_3^{3-}$ and $Eu(dpa)_3^{3-}$ emission spectra that fall within the 300–650 nm wavelength region. All spectra were obtained on aqueous solution samples at 293 K and neutral pH.

Optical absorption and circular dichroism (CD) spectra measured for each of the Co(III) complexes (in aqueous solution) are shown in Figs. 5 and 6. Also shown in Fig. 5 are those parts of the Eu* and Tb* luminescence spectra that fall at emission wavelengths <650 nm. The absorption band centered at approximately 475 nm for each Co(III) complex is assigned to *spin-allowed d–d* transitions that have $^1A_{1g} \rightarrow {}^1T_{1g}$ octahedral (O_h) parentage. This band completely overlaps the highest-energy Tb* emission band ($^7F_6 \leftarrow {}^5D_4$), and it also partially overlaps the next-highest-energy Tb* emission band ($^7F_5 \leftarrow {}^5D_4$). However, there is little or no overlap between this absorption band and any of the Eu* emission lines (assigned to $^7F_{1,2} \leftarrow {}^5D_0$ transitions). These observations suggest that parts of the energy-level manifold derived from the $^1T_{1g}$ electronic excited state of Co^{3+} can satisfy the resonance conditions for Tb*-to-Co electronic energy transfer; but this manifold does not contain suitable acceptor levels for Eu*-to-Co energy-transfer processes.

Six-coordinate amine complexes of Co^{3+} are known to have *spin-forbidden d–d* transitions that span significant parts of the 550–900-nm spectral region. These transitions are generally too weak to be observed in the absorption spectra of dilute solutions, but they have been studied and characterized in some detail for $Co(NH_3)_6^{3+}$ in single crystals [24]. Their absorption bands overlap several $^7F_J \leftarrow {}^5D_4$(Tb*) and $^7F_J \leftarrow {}^5D_0$(Eu*) emission regions, and their excited-state manifolds can satisfy the resonance conditions for both Tb*-to-Co

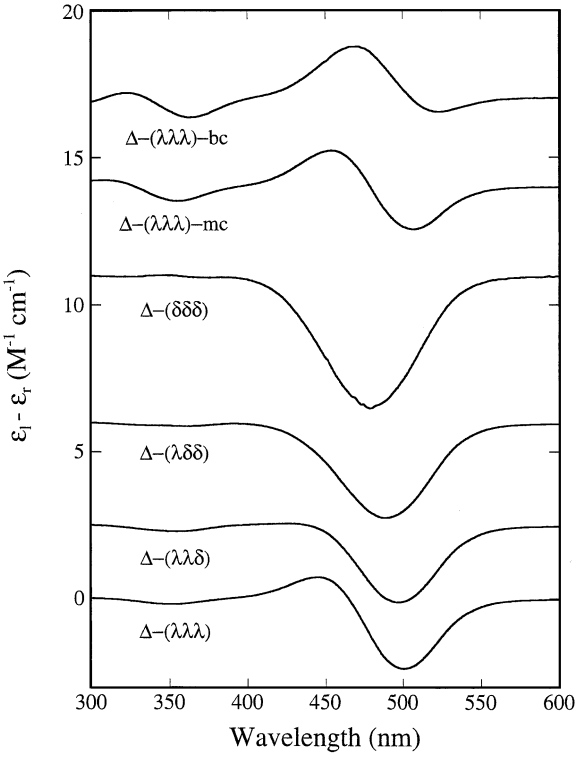

Fig. 6. CD spectra recorded over the 300–600 nm wavelength range for the six Co(III) complexes employed as quenchers in the present study. All spectra were obtained on aqueous solution samples at 293 K and neutral pH.

and Eu*-to-Co energy-transfer processes. Given the low oscillator strengths of the Tb* and Eu* emissive transitions *and* of the resonant Co absorptive transitions, it is nearly certain that these energy-transfer processes involve short-range (contact) interaction mechanisms.

4. Theory and measurement methodology

The general theory underlying the types of experiments carried out in this study has been described in several previous papers, and the optical measurement techniques used in these experiments have also been described previously [11,25,26]. Here we shall review just a few aspects of the general theory and measurement methodologies that are crucial to understanding our experiments and data interpretations.

The samples used in our experiments contain a racemic mixture of chiral luminophores (with enantiomeric structures denoted here by ΛL and ΔL) in solution with a small, optically-resolved concentration of chiral quencher molecules (denoted here by CQ). The luminophores are excited with a pulse of unpolarized light to produce an initially racemic excited-state population (of ΛL^* and ΔL^* enantiomers) which may subsequently evolve to a non-racemic composition in the presence of enantiopreferential quenching actions by the CQ species. Changes in the enantiomeric composition of the excited-state population as a function of time after excitation are determined from TR-CL measurements performed over the lifetime of the excited population. In these TR-CL measurements, light emitted from the excited luminophores is first resolved into left(l)- and right(r)-circularly polarized intensity components, I_l and I_r, which are then wavelength-resolved and measured as functions of time (after excitation at $t \leqslant 0$). The polarization (l/r)-, wavelength (λ)-, and time (t)-resolved emission intensities obtained from these measurements are then combined to obtain the following quantities:

$$I(\lambda,t) = I_l(\lambda,t) + I_r(\lambda,t), \tag{1}$$

$$\Delta I(\lambda,t) = I_l(\lambda,t) - I_r(\lambda,t), \tag{2}$$

$$g_{em}(\lambda,t) = \frac{2\Delta I(\lambda,t)}{I(\lambda,t)} \tag{3}$$

The quantities I and ΔI are often referred to as *total luminescence* (TL) and *circularly polarized luminescence* (CPL) intensities, respectively, and g_{em} is commonly called an *emission dissymmetry factor.*

The wavelength-dependent parts of $I(\lambda,t)$ and $\Delta I(\lambda,t)$ reflect *intrinsic* optical and chiroptical emission properties of the ΛL^* and ΔL^* luminophores, and here we incorporate these properties into four quantities, $F^{\Lambda}_{TL}(\lambda)$, $F^{\Delta}_{TL}(\lambda)$, $F^{\Lambda}_{CPL}(\lambda)$, and $F^{\Delta}_{CPL}(\lambda)$, the details of which are described in Ref. [26]. The time-dependent parts of $I(\lambda,t)$ and $\Delta I(\lambda,t)$ reflect the decay kinetics of the ΛL^* and ΔL^* emitting-state populations and are formulated here in terms of the time-dependent ΛL^* and ΔL^* concentration quantitites, $N^{\Lambda}_{em}(t)$ and $N^{\Delta}_{em}(t)$. Factored into separate wavelength-dependent and time-dependent parts, $I(\lambda,t)$ and $\Delta I(\lambda,t)$ may now be expressed as

$$\begin{aligned} I(\lambda,t) &= F^{\Lambda}_{TL}(\lambda)N^{\Lambda}_{em}(t) + F^{\Delta}_{TL}(\lambda)N^{\Delta}_{em}(t) \\ &= F^{\Lambda}_{TL}(\lambda)N_{em}(t), \end{aligned} \tag{4}$$

$$\begin{aligned} \Delta I(\lambda,t) &= F^{\Lambda}_{CPL}(\lambda)N^{\Lambda}_{em}(t) + F^{\Delta}_{CPL}(\lambda)N^{\Delta}_{em}(t) \\ &= F^{\Lambda}_{CPL}(\lambda)\Delta N_{em}(t), \end{aligned} \tag{5}$$

where $N_{em}(t) = N^{\Lambda}_{em}(t) + N^{\Delta}_{em}(t)$, $\Delta N_{em}(t) = N^{\Lambda}_{em}(t) - N^{\Delta}_{em}(t)$, and we have made use of the following relationships (applicable to optical isomers): $F^{\Lambda}_{TL}(\lambda) = F^{\Delta}_{TL}(\lambda)$ and $F^{\Lambda}_{CPL}(\lambda) = -F^{\Delta}_{CPL}(\lambda)$. Insertion of Eqs. (4) and (5) into Eq. (3) yields the following expressions for emission dissymmetry:

$$\begin{aligned} g_{em}(\lambda,t) &= \left(\frac{2F^{\Lambda}_{CPL}(\lambda)}{F^{\Lambda}_{TL}(\lambda)}\right) \\ &\quad \times \left(\frac{\Delta N_{em}(t)}{N_{em}(t)}\right) = g^{\Lambda}_{em}(\lambda)\eta_{em}(t), \end{aligned} \tag{6}$$

where $\eta_{em}(t)$ gives the time-development of *enantiomeric excess* in the overall luminophore emitting-state population, and $g^{\Lambda}_{em}(\lambda)$ is the emission dissymmetry that would be observed for a fully

resolved emitting-state population of ΛL^* enantiomers.

All of the enantiopreferential quenching information derived from our TR-CL experiments comes from the time-dependent parts of $I(\lambda,t)$, $\Delta I(\lambda,t)$, and $g_{em}(\lambda,t)$, which reflect sums and/or differences of the $N^{\Lambda}_{em}(t)$ and $N^{\Delta}_{em}(t)$ concentration quantities. The rate processes relevant to a purely phenomenological analysis of N^{Λ}_{em} and N^{Δ}_{em} time dependence are:

(a) excited-state enantiomer interconversions

$$\Lambda L^* \xrightarrow{k_c^{\Lambda}} \Delta L^*, \quad \Delta L^* \xrightarrow{k_c^{\Delta}} \Lambda L$$

$$k_c^{\Lambda} = k_c^{\Delta} = k_c$$

(b) radiative and nonradiative decay of ΛL^* and ΔL^* in the absence of any quencher (CQ) actions

$$\Lambda L^* \xrightarrow{k_o^{\Lambda}} \Lambda L + E_r + E_{nr}, \quad \Delta L^* \xrightarrow{k_o^{\Delta}} \Delta L + E_r + E_{nr},$$

$$k_o^{\Lambda} = k_o^{\Delta} = k_o$$

(where E_r and E_{nr} denote radiative and nonradiative energies, respectively),

(c) deexcitation of ΛL^* and ΔL^* via bimolecular quenching events

$$\Lambda L^* + CQ \xrightarrow{k_q^{\Lambda}} \Lambda L + CQ^* \downarrow \text{fast} \; CQ$$

$$\Delta L^* + CQ \xrightarrow{k_q^{\Delta}} \Delta L + CQ^* \downarrow \text{fast} \; CQ$$

Based on the rate processes shown in (a), (b) and (c) above, the differential rate equations for $N^{\Lambda}_{em}(t)$ and $N^{\Delta}_{em}(t)$ decay may be written as

$$-\frac{dN^{\Lambda}_{em}(t)}{dt} = (k_o + k_c + k_q^{\Lambda}[CQ])N^{\Lambda}_{em}(t) - k_c N^{\Delta}_{em}(t), \tag{7}$$

$$-\frac{dN^{\Delta}_{em}(t)}{dt} = (k_o + k_c + k_q^{\Delta}[CQ])N^{\Delta}_{em}(t) - k_c N^{\Lambda}_{em}(t), \tag{8}$$

where [CQ] denotes the ground-state quencher concentration, which can be assumed to be constant under the specified conditions that $CQ^* \rightarrow CQ$ relaxation processes are much faster than $L^* \rightarrow L$ decay processes. These equations may be integrated and then combined to obtain the following expressions for the sums and differences of $N^{\Lambda}_{em}(t)$ and $N^{\Delta}_{em}(t)$:

$$N_{em}(t) = N^{\Lambda}_{em}(t) + N^{\Delta}_{em}(t) = \frac{N_{em}(0)}{2Z}\left\{(Z - 2k_c)e^{-t/\tau_1} + (Z + 2k_c)e^{-t/\tau_2}\right\}, \tag{9}$$

$$\Delta N_{em}(t) = N^{\Lambda}_{em}(t) - N^{\Delta}_{em}(t) = \frac{N_{em}(0)}{2Z}\{k_{dq}[CQ]e^{-t/\tau_1} - k_{dq}[CQ]e^{-t/\tau_2}\}, \tag{10}$$

where

$$k_{dq} = k_q^{\Lambda} - k_q^{\Delta}, \quad Z = \left[(k_{dq}[CQ])^2 + 4k_c^2\right]^{1/2},$$

and

$$\frac{1}{\tau_1} = k_o + k_c + k_q^m[CQ] + Z/2, \tag{11}$$

$$\frac{1}{\tau_2} = k_o + k_c + k_q^m[CQ] - Z/2, \tag{12}$$

where $k_q^m = (k_q^{\Delta} + k_q^{\Lambda})/2$. In the derivation of Eqs. (9) and (10) from Eqs. (7) and (8), the initial concentrations of ΛL^* and ΔL^* were set equal (i.e. $N^{\Lambda}_{em}(0) = N^{\Delta}_{em}(0)$) to reflect the racemic composition of the initially prepared luminophore excited-state population.

Eqs. (9) and (10) may now be combined with Eqs. (4)–(6) to obtain the following expressions for $I(\lambda,t)$, $\Delta I(\lambda,t)$, and $g_{em}(\lambda,t)$:

$$I(\lambda,t) = I_1(\lambda)e^{-t/\tau_1} + I_2(\lambda)e^{-t/\tau_2}, \tag{13}$$

$$\Delta I(\lambda,t) = \Delta I(\lambda)[e^{-t/\tau_1} - e^{-t/\tau_2}], \quad (14)$$

$$g_{em}(\lambda,t) = g_{em}^{\Lambda}(\lambda)\left\{\frac{k_{dq}[CQ]\tanh(-Zt/2)}{Z + 2k_c\tanh(Zt/2)}\right\}, \quad (15)$$

where

$$I_1(\lambda) = F_{TL}^{\Lambda}(\lambda)N_{em}(0)[Z - 2k_c]/2Z,$$

$$I_2(\lambda) = F_{TL}^{\Lambda}(\lambda)N_{em}(0)[Z + 2k_c]/2Z,$$

$$\Delta I(\lambda) = F_{CPL}^{\Lambda}(\lambda)N_{em}(0)k_{dq}[CQ]/2Z,$$

and the quantity inside the braces in Eq. (15) corresponds to the *enantiomeric excess function* $\eta_{em}(t) = \Delta N_{em}(t)/N_{em}(t)$. Note from Eqs. (13) and (14) that $I(\lambda,t)$ will decay smoothly from a value of $I_1(\lambda) + I_2(\lambda) = F_{TL}^{\Lambda}N_{em}(0)$ at $t = 0$ to a value of 0 at long times ($t \rightarrow \infty$) after excitation, whereas $\Delta I(\lambda,t)$ will have an initial value of 0, grow to a maximum (in magnitude) at $t = [\tau_1\tau_2/(\tau_2 - \tau_1)]\ln(\tau_2\tau_1)$, and then decay to 0 at long times after excitation. The emission dissymmetry factor $g_{em}(\lambda,t)$ will have an initial value of 0, then grow in magnitude towards a 'limiting' value of

$$g_{em}(\lambda,\infty) = -g_{em}^{\Lambda}(\lambda)\left\{\frac{k_{dq}[CQ]}{Z + 2k_c}\right\}, \quad (16)$$

as $t \rightarrow \infty$.

Parametric fits of $I(\lambda,t)$, $\Delta I(\lambda,t)$ and $g_{em}(\lambda,t)$ data to Eqs. (13)–(15) yield all the information needed to evaluate the rate parameters of principal interest in this study. These rate parameters are the *mean quenching constant* (k_q^m) and the *enantiodifferential quenching constant* (k_{dq}), which may be used to determine the *enantiospecific quenching constants* (k_q^{Λ} and k_q^{Δ}) from the relations:

$$k_q^{\Lambda} = k_q^m + (1/2)k_{dq}, \quad k_q^{\Delta} = k_q^m - (1/2)k_{dq}. \quad (17)$$

The 'unquenched' luminescence decay constant (k_o) and the enantiomer interconversion rate constant (k_c) may also be evaluated from parametric analyses of the TR-CL data obtained in the quenching experiments, but in practice the values of these rate constants are determined from separate sets of experiments carried out on samples that contain no quencher species.

5. Experimental section

5.1. Sample preparation

All of the luminescence quenching measurements reported in this study were carried out on *neutral* H_2O and D_2O solution samples that contained a 10 mM concentration of either $Eu(dpa)_3^{3-}$ or $Tb(dpa)_3^{3-}$ complexes (the luminophores) and a 10 μM concentration of chiral Co(III) complexes (the quenchers). Stock solutions of the luminophores and the quencher systems were prepared separately, and these solutions were then used in preparing the samples on which the quenching experiments were performed.

Aqueous solutions of $Eu(dpa)_3^{3-}$ and $Tb(dpa)_3^{3-}$ were prepared by reaction of the appropriate lanthanide carbonate, $Eu_2(CO_3)_3$ or $Tb_2(CO_3)_3$, with six equivalents of dipicolinic acid and three equivalents of Na_2CO_3 in H_2O. The resulting solutions were heated mildly to drive off excess CO_2 and were then brought to pH 7 by dropwise addition of 1 M Na_2CO_3. Portions of these solutions were then evaporated to dryness (under high vacuum), and the resulting solids were dissolved in D_2O to form stock D_2O solutions of $Eu(dpa)_3^{3-}$ and $Tb(dpa)_3^{3-}$.

Four of the six Co(III) complexes used as quenchers in this study are structural diastereomers with ligand compositions and elements of structural chirality specified by Δ-(λλλ)-$[Co(R,R\text{-dach})_3]^{3+}$, Δ-(λλδ)-$[Co(R,R\text{-dach})_2(S,S\text{-dach})]^{3+}$, Δ-(λδδ)-$[Co(R,R\text{-dach})(S,S\text{-dach})_2]^{3+}$, and Δ-(δδδ)-$[Co(S,S\text{-dach})_3]^{3+}$, where *R,R*-dach and *S,S*-dach denote the 1(*R*),2(*R*) and 1(*S*),2(*S*) optical isomers of *trans*-1,2-diaminocyclohexane (dach) ligand molecules. These complexes were synthesized and their diastereomeric structures were resolved and characterized following methods reported by Harnung et al. and by Geue et al. [27–29]. Additional details regarding the synthesis, resolution, and structural characterization of these complexes can be found in Ref. [30].

The two additional Co(III) complexes used as quenchers have structures in which either one or both of the trigonal faces of Δ-(λλλ)-[Co(*R,R*-dach)$_3$]$^{3+}$ are capped by a tris(methylene)amino group attached to three nitrogen atoms of the [CoN$_6$]$^{3+}$ coordination core. These complexes were prepared together in a single sequence of reactions, and the *mono-capped* and *bi-capped* complexes in the product mixture were then separated using cation-exchange column chromatography. The structures of the complexes were characterized by X-ray crystallography, ^{1}H and ^{13}C NMR spectroscopy, and elemental analysis. Details regarding the preparation and characterization of these complexes are given in Ref. [30].

5.2. Spectroscopic measurements

Optical absorption spectra were obtained using a Cary Model 5E UV/Vis/NIR absorption spectrophotometer, and CD measurements were performed using a Jasco Model J-720 CD/absorption spectrophotometer. All TR-CL measurements were carried out using instrumentation and techniques developed in the authors' laboratory at the University of Virginia.

The TR-CL measurements were performed on solution samples contained in $1\times1\times3$ cm^3 fluorescence cuvettes retained in a thermostatted cuvette holder. The excitation source was a cw argon-ion laser (Coherent Innova 90-6) tuned to either 488.0 nm output (for Tb(dpa)$_3^{3-}$ excitation) or 465.8 nm output (for Eu(dpa)$_3^{3-}$ excitation). The cw output from the laser was chopped with a Stanford Research Systems SR-540 mechanical chopper to create excitation pulses of 30 μs duration at a repetition rate of 100 Hz. The excitation pulses were directed into the solution sample through the bottom of the sample cuvette, and luminescence from the sample was collected from one side of the cuvette, along a direction perpendicular to the direction of excitation. The collected luminescence was then passed through a photoelastic modulator (PEM) and a linear polarizer, which together function as a dynamic circular-polarization analyzer unit. This analyzer unit alternately passed left- and right-circularly polarized light during its 3 μs periods of full-depth modulation. The modulation frequency of the PEM was 50 kHz, corresponding to a period of 20 μs. The light passed through the circular-polarization analyzer unit was then focused onto the entrance slit of a single-grating monochromator tuned to pass light of either 543.7 nm wavelength (for Tb* luminescence) or 594.8 nm wavelength (for Eu* luminescence). The intensity of the light exiting the monochromator was measured using an RCA-C31034 photomultiplier tube and photon-counting electronics. Photon counts were collected in 3-μs bins which were synchronized to the modulation cycle of the PEM. These bins were stored in arrays in a computer along with their time and circular-polarization information. The left- and right-circularly polarized counts occurring in each 20-μs modulation cycle were then added to obtain the desired $I(\lambda,t)=I_l(\lambda,t)+I_r(\lambda,t)$ intensity data, and were subtracted to obtain the $\Delta I(\lambda,t)=I_l(\lambda,t)-I_r(\lambda,t)$ intensity data. The excitation pulses occurred randomly in either half of the PEM modulation cycle, and the counting bins were sequenced such that the left–right–left–right order was reversed for each successive excitation-luminescence decay measurement. Each of the I and ΔI decay curves used in our analyses of excited-state decay kinetics represented a statistical average of data acquired from at least 10^6 excitation-luminescence decay measurements. Marquardt-based non-linear least-squares fitting routines were used to fit the $I(\lambda,t)$, $\Delta I(\lambda,t)$, and $g_{em}(\lambda,t)=2\Delta I(\lambda,t)/I(\lambda,t)$ data to Eqs. (13)–(15), with appropriate modifications for dark counts present in the data.

6. Results

6.1. General

In all of the experiments performed in this study, the spectral dispersion characteristics of the Eu* and Tb* luminescence were observed to be identical for solution samples prepared *with* and *without* inclusion of quencher molecules. Furthermore, the CPL generated by enantiodifferential quenching exhibited spectral dispersion characteristics identical to those observed in CPL generated by circularly polarized excitation of Eu(dpa)$_3^{3-}$ and

$Tb(dpa)_3^{3-}$ complexes in the absence of any chiral reagents. These results indicate that the luminescence observed in our quenching experiments derives entirely from Eu* or Tb* complexes that are free of any perturbations by the quencher molecules. The quenchers alter the decay kinetics of the Λ and Δ luminophore excited-state populations, and thereby reduce the mean lifetimes and intensities of the sample luminescence, but they have no effects on the spectral dispersion characteristics of the sample luminescence. Chiroptical luminescence spectra of $Eu(dpa)_3^{3-}$ and $Tb(dpa)_3^{3-}$ complexes (in the presence *and* absence of CQ molecules) have been presented in several previous papers [9,26] and will not be shown again here. All of the results given in the present paper were obtained from TR-CL experiments in which left- and right-circularly polarized emission intensities were measured at either λ = 594.8 nm (for the Eu* luminophores) or λ = 543.7 nm (for the Tb* luminophores).

Examples of *time-resolved* TL ($I = I_l + I_r$), CPL ($\Delta I = I_l - I_r$), and emission dissymmetry ($g_{em} = 2\Delta I/I$) data obtained from our TR-CL measurements are shown in Fig. 7. Note from the data shown in this figure that the emission dissymmetry has an initial value of *zero* (diagnostic of an initially *racemic* excited-state population of luminophores), and then it grows in magnitude with a time dependence that reflects the evolution of enantiomeric excess in the luminophore excited-state population (due to enantiodifferential quenching kinetics). The time dependence of g_{em} conforms to the rate expression given by Eq. (15); the time dependence of CPL intensity (ΔI) follows the double-exponential rate expression given by Eq. (14); and the time dependence of the TL intensity (I) follows the double-exponential rate expression given by Eq. (13).

Fits of the TR-CL data to Eqs. (13)–(15) yielded values for the τ_1,τ_2 and Z parameters, which were then combined with known (independently measured) values of k_o and k_c to determine k_q^m and k_{dq}. The k_o data relevant to this study can be found in Refs. [9–11], and the k_c data can be found in Ref. [23] (*or* generated from the results shown in Table 1 of the present paper). Over the 273–308 K temperature range represented in this

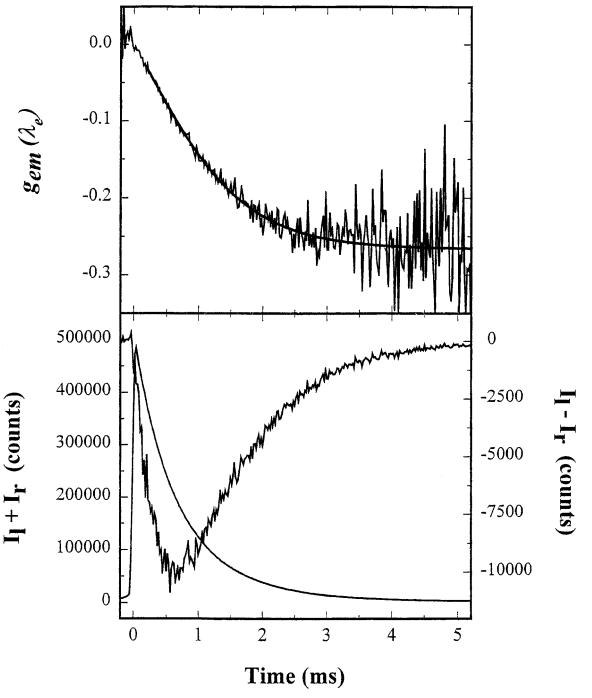

Fig. 7. TR-CL data for 10 mM $Eu(dpa)_3^{3-}$ in H_2O with 5 μM Δ-(λλλ)-$[Co(R,R\text{-dach})_3]^{3+}$. The bottom frame shows the time-resolved TL ($I_L + I_R$, smooth trace) and CPL ($I_L - I_R$, noisy trace). The top frame shows the time-resolved emission dissymmetry data calculated from the CPL and TL data given in the bottom frame. The heavy trace in the top frame represents a fit of the g_{em} data to Eq. (15). The sample was excited with chopped radiation at 465.8 nm, and emission intensity was monitored at 594.8 nm. Sample temperature was 293 K.

study, k_o varies from 611 to 624 s^{-1} for Eu* in H_2O, from 314 to 321 s^{-1} for Eu* in D_2O, from 476 to 481 s^{-1} for Tb* in H_2O, and from 446 to 450 s^{-1} for Tb* in D_2O. Over this temperature range the k_c values are in all cases < 50 s^{-1}.

Throughout the remainder of this paper we will use the chirality labels Δ-(λλλ), Δ-(λλδ), Δ-(λδδ), and Δ-(δδδ) to distinguish between the four Δ-$[Co(R,R\text{-dach})_{3-y}(S,S\text{-dach})_y]$ ($y = 0$, 1, 2 or 3) complexes, and we use the notation Δ-(λλλ)-*mc* and Δ-(λλλ)-*bc* to identify, respectively, the *mono-capped* and *bi-capped* derivatives of Δ-$[Co(R,R\text{-dach})_3]^{3+}$.

6.2. Quenching kinetics at 293 K

The enantiospecific quenching constants k_q^σ ($\sigma \equiv \Lambda$ or Δ) and quenching efficiencies ε_q^σ deter-

Table 2
Rate constants, quenching efficiencies and enantioselectivity parameters determined from TR-CL measurements of enantiodifferential excited-state quenching kinetics in H_2O and D_2O solution samples at 293 K[a,b]

Solvent	Quencher[c]	$k_q^\sigma \times 10^{-7}$ ($M^{-1}\,s^{-1}$)				$\varepsilon_q^\sigma \times 100$				E_q	
		Λ-Eu*	Δ-Eu*	Λ-Tb*	Δ-Tb	Λ-Eu*	Δ-Eu*	Λ-Tb*	Δ-Tb*	Eu*	Tb*
H_2O	Δ-(δδδ)	0.44	3.16	0.56	3.20	6.6	33.8	10.5	40.2	−0.76	−0.70
	Δ-(λδδ)	2.22	9.60	2.81	9.83	26.4	60.8	37.2	67.3	−0.62	−0.56
	Δ-(λλδ)	4.39	5.53	5.25	6.26	41.5	47.1	52.4	56.8	−0.11	−0.09
	Δ-(λλλ)	11.41	3.19	12.61	4.13	64.8	34.0	72.6	46.4	0.56	0.51
	Δ-(λλλ)-*mc*	8.43	2.22	10.31	3.71	57.6	26.4	68.4	43.8	0.58	0.47
	Δ-(λλλ)-*bc*	3.37	2.15	6.86	4.37	35.2	25.7	59.0	47.8	0.22	0.22
D_2O	Δ-(δδδ)	0.34	2.64	0.40	1.91	9.7	45.4	8.2	29.9	−0.77	−0.65
	Δ-(λδδ)	1.99	8.78	3.12	11.94	38.5	73.4	41.1	72.8	−0.63	−0.59
	Δ-(λλδ)	3.64	4.64	6.21	7.90	53.4	59.3	58.1	63.9	−0.12	−0.12
	Δ-(λλλ)	9.50	2.84	14.83	4.92	74.9	47.2	76.8	52.4	0.54	0.50
	Δ-(λλλ)-*mc*	6.51	1.88	10.55	3.71	67.2	37.2	70.2	45.4	0.55	0.48
	Δ-(λλλ)-*bc*	2.16	1.39	5.12	3.17	40.4	30.4	53.4	41.5	0.22	0.24

[a] All measurements were carried out on neutral aqueous (H_2O or D_2O) solution samples in which the $Eu(dpa)_3^{3-}$ or $Tb(dpa)_3^{3-}$ luminophore concentration was 10 mM and the cobalt quencher concentration was 10 μM.

[b] The rate constants $k_q^\sigma(\sigma \equiv \Lambda \text{ or } \Delta)$ are defined according to the expressions given in Section 4; the quenching efficiency parameters $\varepsilon_q^\sigma(\sigma \equiv \Lambda \text{ or } \Delta)$ are defined according to Eq. (18); and the quenching enantioselectivity parameter E_q is defined according to Eq. (19).

[c] See Section 2.2 for a description of quencher notation and labeling schemes.

mined from TR-CL measurements carried out on solution samples at 293 K are shown in Table 2. The quenching efficiencies are defined according to

$$\varepsilon_q^\sigma = \frac{k_q^\sigma[CQ]}{k_o + k_q^\sigma[CQ]} = 1 - \frac{k_o}{k_o + k_q^\sigma[CQ]}, \tag{18}$$

and they correspond to the fractional contribution of ΛL^*−CQ (or ΔL^*−CQ) quenching actions to the total rate of ΛL^* (or ΔL^*) deactivation. A significant part of the solvent (H_2O vs. D_2O) and luminophore (Eu* vs. Tb*) dependence exhibited by the ε_q^σ data derives from the solvent and luminophore dependence of the k_o rate constant. At 293 K, the relevant values of k_o are: 620 s^{-1} for Eu* in H_2O; 318 s^{-1} for Eu* in D_2O; 477 s^{-1} for Tb* in H_2O; and 447 s^{-1} for Tb* in D_2O. All of the results shown in Table 2 were obtained from measurements on solution samples in which the quencher concentration was $[CQ] = 10$ μM.

The E_q quantities shown in Table 2 are defined by

$$E_q = \frac{k_q^\Lambda - k_q^\Delta}{k_q^\Lambda + k_q^\Delta} = \frac{k_{dq}}{2k_q^m}, \tag{19}$$

and following previous practice we shall refer E_q as a quenching *enantioselectivity* parameter. This parameter can have values between +1 and −1, and its magnitude and sign provide useful indicators of the *degree* and *sense* of enantioselectivity in the quenching processes.

We note from the results shown in Table 2 that the E_q(Eu*) and E_q(Tb*) data sets are very similar with respect to quencher-dependent trends, and that within each of these data sets the E_q values exhibit a striking dependence on relatively small incremental changes in quencher structure. Perhaps most striking is the observation that the Δ-(λλλ), Δ-(λλλ)-*mc*, and Δ-(λλλ)-*bc* quenchers produce E_q values that are opposite in sign to those produced by the Δ-(δδδ), Δ-(λδδ), and Δ-(λλδ) quenchers. The latter exhibit a preference for Δ-

Ln* (over Λ-Ln*) quenching interactions, whereas the former exhibit a preference for Λ-Ln* (over Δ-Ln*) quenching interactions. These results give clear evidence that both the degree and sense of chiral recognition and discrimination manifested in the quenching processes are in large part determined by the chiral structural elements associated with the *individual* ligands and chelate rings of the quencher complexes. The configurational chirality defined by the helicity of the chelate-ring distribution about the metal center in these complexes appears to have a much less significant influence on chiral recognition and discrimination.

In our enantiodifferential quenching experiments, the time development of enantiomeric excess in the luminophore emitting-state population is given by

$$\eta_{em}(t) = \frac{\Delta N_{em}(t)}{N_{em}(t)} = \frac{(k_q^{\Lambda} - k_q^{\Delta})[CQ]\tanh(-Zt/2)}{Z + 2k_c\tanh(Zt/2)}, \quad (20)$$

where $\Delta N_{em}(t)$ and $N_{em}(t)$ are defined as shown in Eqs. (9) and (10), and $Z = [(k_q^{\Lambda} - k_q^{\Delta})^2[CQ]^2 + 4k_c^2]^{1/2}$. Plots of $\eta_{em}(t)$ are shown in Fig. 8 for Eu* quenching in H_2O solution samples at 293 K (where in each case, $[CQ] = 10\ \mu M$). These plots give a particularly clear illustration of the remarkably large differences between the enantiopreferential quenching kinetics observed for the six quencher systems.

6.3. Temperature dependence of quenching kinetics

TR-CL measurements were performed on each of the 12 luminophore–quencher systems (in both H_2O and D_2O solutions) at eight different sample temperatures between 273 and 308 K, with $\Delta T = 5$ K intervals between the different temperatures. Over this temperature range the spectral dispersion characteristics of the Eu* and Tb* luminescence show no detectable temperature dependence and no solvent (H_2O vs. D_2O) dependence. However, in each case the quenching constants evaluated from our TR-CL measurements show temperature-dependent behavior that can be represented quite well by either Arrhenius or Eyring equations of the form:

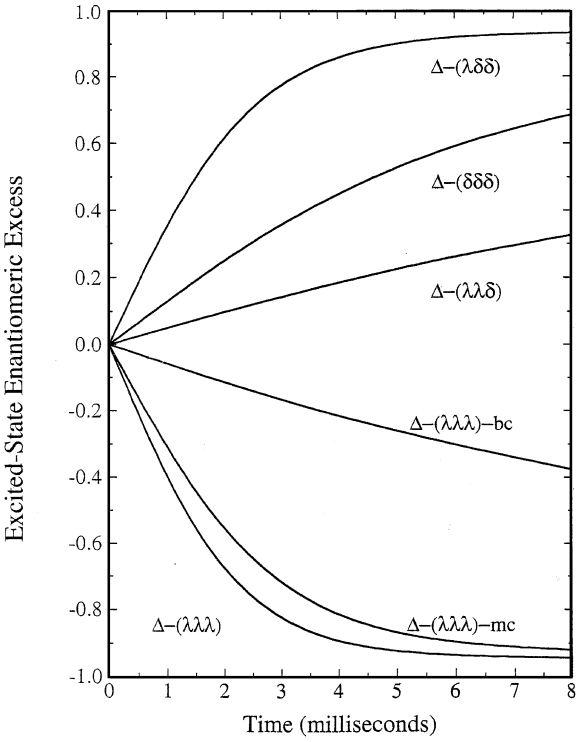

Fig. 8. Time development of enantiomeric excess produced in the $Eu(dpa)_3^{3-}$ ($^5D_0$) excited-state population by the enantiopreferential quenching actions of the six different chiral Co(III) complexes. The plots shown in this figure are based on measurements performed on aqueous (H_2O) solution samples at 293 K.

$$\ln k_q^{\sigma} = \ln A^{\sigma} - \frac{E_a^{\sigma}}{RT}, \quad \text{(Arrhenius)} \quad (21)$$

$$\ln\left(\frac{k_q^{\sigma}}{T}\right) = \ln\left(\frac{k_B}{h}\right) + \frac{\Delta S_{\sigma}^{\#}}{R} - \frac{\Delta H_{\sigma}^{\#}}{RT}, \quad \text{(Eyring)} \quad (22)$$

where $\sigma \equiv \Lambda$ or Δ (which distinguishes between Λ-Ln* vs. Δ-Ln* quenching processes); the k_q^{σ} are the enantiospecific quenching constants; A^{σ} and E_a^{σ} are the Arrhenius preexponential and activation-energy parameters, respectively; and $\Delta S_{\sigma}^{\#}$ and $\Delta H_{\sigma}^{\#}$ are phenomenological activation entropy and enthalpy parameters.

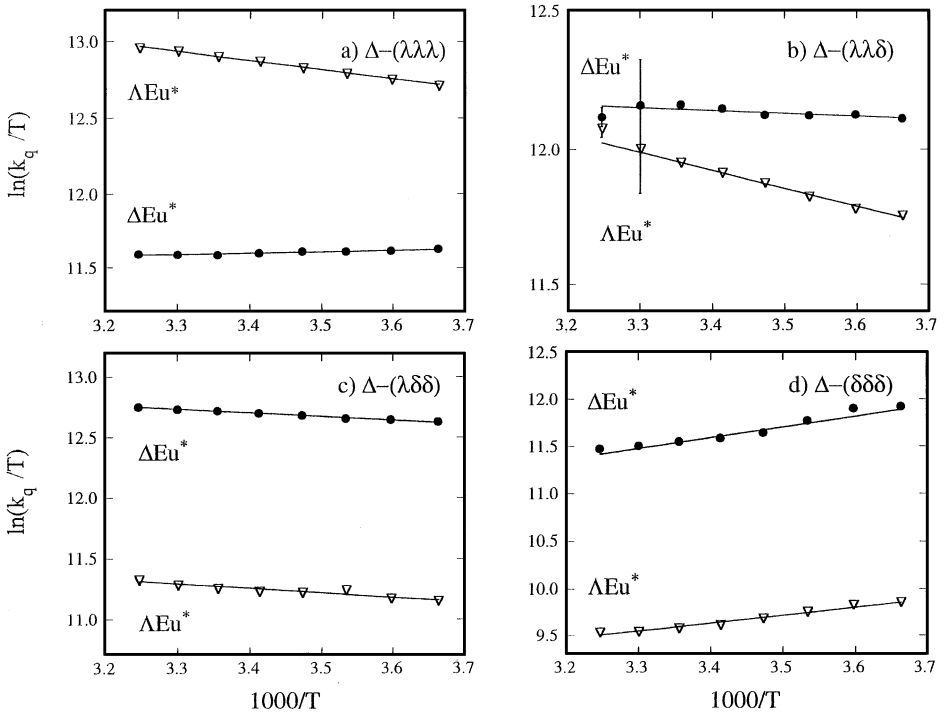

Fig. 9. Plots of $\ln(k_q^\sigma/T)$ vs. $1/T$, using quenching constant data obtained over the 273–308 K temperature range for aqueous (H_2O) solution samples that contained a 10 mM concentration of $Eu(dpa)_3^{3-}$ and a 10 μM concentration of the (a) Δ-(λλλ), (b) Δ-(λλδ), (c) Δ-(λδδ), or (d) Δ-(δδδ) diastereomeric structures of $[Co(R,R\text{-dach})_{3-y}(S,S\text{-dach})_y]^{3+}$ ($y=0$, 1, 2 or 3). The straight lines shown in the figure were obtained from error-weighted least-squares fits of the data points to Eq. (22).

In Figs. 9–11 we show $\ln(k_q^\sigma/T)$ vs. $1/T$ (Eyring) plots that encompass all the k_q^σ rate-constant data obtained from our measurements on H_2O solution samples. Fits of the data points in each plot to Eq. (22) yielded the $\Delta H_\sigma^\#$ and $\Delta S_\sigma^\#$ parameter values shown in the upper halves of Tables 3 and 4. Each data fit took into account uncertainties in the measured values of k_q^σ. Eyring plots of the k_q^σ data obtained from our measurements on D_2O solution samples are not shown here, but the $\Delta H_\sigma^\#$ and $\Delta S_\sigma^\#$ parameter values derived from analyses of that data are listed in the bottom halves of Tables 3 and 4. Also listed in Tables 3 and 4 are values of the *enantiodifferential activation parameters*: $\Delta\Delta H^\# = \Delta H_\Lambda^\# - \Delta H_\Delta^\#$; $\Delta\Delta S^\# = \Delta S_\Lambda^\# - \Delta S_\Delta^\#$; and $\Delta\Delta G^\# = \Delta\Delta H^\# - T\Delta\Delta S^\#$ (evaluated at $T=293$ K).

Expressed in terms of the enantiodifferential activation parameters, the temperature dependence of the quenching enantioselectivity parameter (E_q) is given by

$$E_q = \tanh\left(\frac{\Delta\Delta S^\#}{2R} - \frac{\Delta\Delta H^\#}{2RT}\right) = \tanh\left(\frac{-\Delta\Delta G^\#}{2RT}\right). \quad (23)$$

Figs. 12 and 13 show E_q vs. T plots in which the data points correspond to experimentally measured values of E_q and the solid lines represent plots of Eq. (23), with the relevant values of $\Delta\Delta S^\#$ and $\Delta\Delta H^\#$ taken from Tables 3 and 4. All the data shown in these figures are from measurements carried out on H_2O solution samples.

7. Discussion

7.1. General mechanistic considerations

Mechanistic pathways for the types of compet-

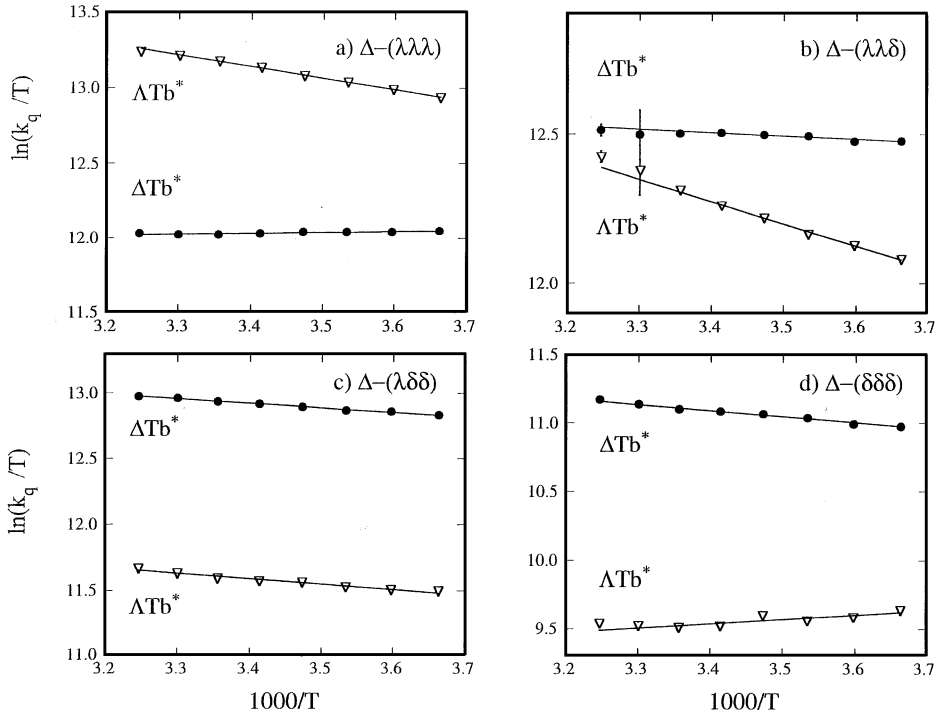

Fig. 10. Plots of $\ln(k_q^{\alpha}/T)$ vs. $1/T$, using quenching constant data obtained over the 273–308 K temperature range for aqueous (H_2O) solution samples that contained a 10 mM concentration of $Tb(dpa)_3^{3-}$ and a 10 μM concentration of the (a) Δ-(λλλ), (b) Δ-(λλδ), (c) Δ-(λδδ), or (d) Δ-(δδδ) diastereomeric structures of $[Co(R,R\text{-dach})_{3-y}(S,S\text{-dach})_y]^{3+}$ ($y=0$, 1, 2 or 3). The straight lines shown in the figure were obtained from error-weighted least-squares fits of the data points to Eq. (22).

ing ΛL* and ΔL* quenching processes investigated in this study have been considered in some detail in several of our previous papers [11,12,25]. Here we will focus only on those parts of the previously described mechanistic models and pathways that are essential to interpreting or rationalizing the enantio-differential quenching kinetics observed for the systems examined in the present study. In these systems, quenching occurs via electronic energy transfer (from L* to CQ) in transient L*–CQ contact pairs formed during diffusional encounters between the excited luminophores and ground-state quencher species in solution. The key steps to consider in analyses of the enantiodifferential quenching kinetics are shown in the following two sequences of interaction/reaction rate processes:

$$\Lambda L^* + CQ \underset{k_{d^\Lambda}}{\overset{k_{a^\Lambda}}{\rightleftarrows}} (\Lambda L^* - CQ) \underset{k_{-e^\Lambda}}{\overset{k_{e^\Lambda}}{\rightleftarrows}} (\Lambda L - CQ^*) \xrightarrow{k_{x^\Lambda}} \Lambda L + CQ, \tag{24}$$

$$\Delta L^* + CQ \underset{k_{d^\Delta}}{\overset{k_{a^\Delta}}{\rightleftarrows}} (\Delta L^* - CQ) \underset{k_{-e^\Delta}}{\overset{k_{e^\Delta}}{\rightleftarrows}} (\Delta L - CQ^*) \xrightarrow{k_{x^\Delta}} \Delta L + CQ, \tag{25}$$

where the last step shown in each sequence is defined to encompass all processes that deactivate the (L–CQ*) species to ground-state L and CQ species. Analyses of these two reaction sequences, using steady-state approximations for the concentrations of (L*–CQ) and (L–CQ*) species, yield

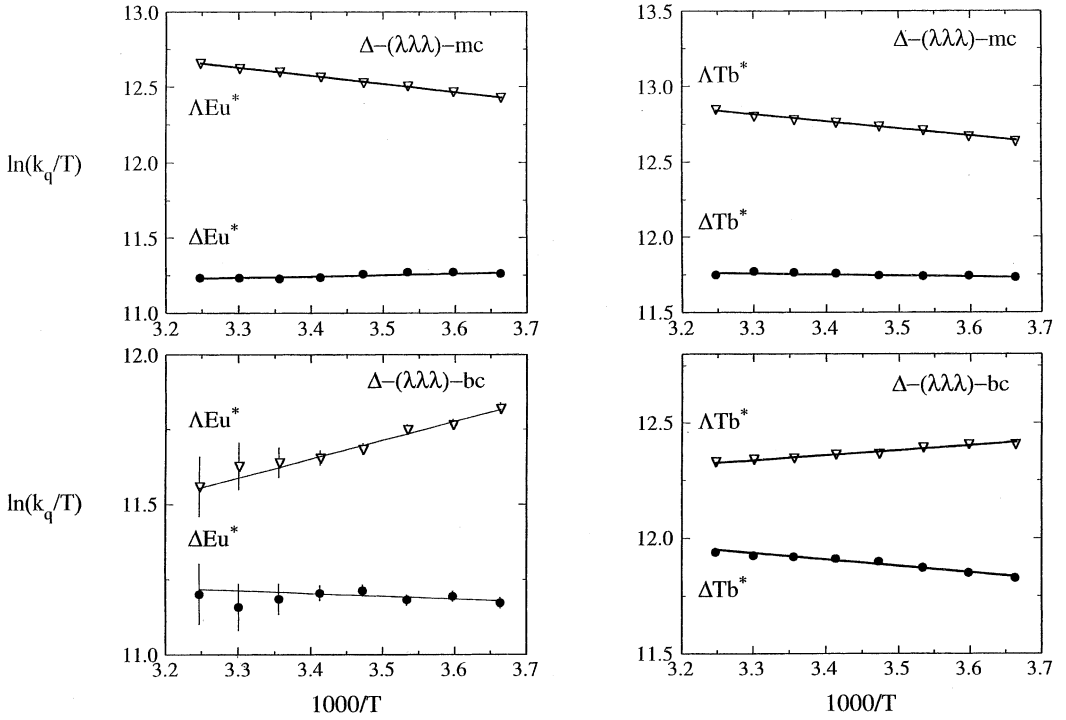

Fig. 11. Plots of $\ln(k_q^{\sigma}/T)$ vs. $1/T$, using quenching constant data obtained over the 273–308 K temperature range for aqueous (H_2O) solution samples that contained a 10 mM concentration of *either* $Eu(dpa)_3^{3-}$ or $Tb(dpa)_3^{3-}$, and a 10 μM concentration of *either* the Δ-(λλλ)-*mc or* the Δ-(λλλ)-*bc* Co(III) complexes.

Table 3
Thermal activation parameters determined for Λ-Eu* and Δ-Eu* quenching processes in H_2O and D_2O solution samples[a]

Solvent	Quencher	$\Delta H_{\sigma}^{\#}$ (kJ mol^{-1})[b]		$\Delta S_{\sigma}^{\#}$ (J mol^{-1} K^{-1})[b]		Enantiodifferential activation parameters[c]		
		Λ-Eu*	Δ-Eu*	Λ-Eu*	Δ-Eu*	$\Delta\Delta H^{\#}$ (kJ mol^{-1})	$\Delta\Delta S^{\#}$ (J mol^{-1} K^{-1})	$\Delta\Delta G^{\#}$ (kJ mol^{-1}) at 293 K
H_2O	Δ-(δδδ)	−7.0(4)	−9.42(5)	−141(1)	−133.2(2)	2.4(4)	−8(2)	4.7(4)
	Δ-(λδδ)	3.1(2)	2.54(4)	−93.3(5)	−83.3(1)	0.6(2)	−10.0(5)	3.5(2)
	Δ-(λλδ)	5.5(2)	0.9(1)	−79.8(7)	−93.7(5)	4.6(2)	13.9(9)	0.5(2)
	Δ-(λλλ)	4.96(4)	−0.7(1)	−73.6(1)	−103.6(5)	5.7(1)	30.0(5)	−3.1(1)
	Δ-(λλλ)-*mc*	4.53(4)	−0.7(1)	−77.6(1)	−106.6(4)	5.2(1)	29.0(5)	−3.3(1)
	Δ-(λλλ)-*bc*	−5.3(1)	0.8(7)	−119(2)	−102(3)	−6.1(9)	−17(3)	−1.1(9)
D_2O	Δ-(δδδ)	−5.4(6)	−7.9(1)	−138(2)	−129.5(2)	2.5(6)	−8(2)	4.8(6)
	Δ-(λδδ)	3.0(1)	2.77(2)	−94.7(3)	−83.2(1)	0.2(1)	−11.5(3)	3.6(1)
	Δ-(λλδ)	5.5(1)	0.0(1)	−81.2(5)	−97.9(4)	5.5(2)	16.7(6)	0.6(2)
	Δ-(λλλ)	5.71(3)	−1.25(8)	−72.5(1)	−106.4(3)	6.96(9)	33.9(3)	−2.98(9)
	Δ-(λλλ)-*mc*	4.97(3)	−0.9(1)	−78.2(1)	−108.7(4)	5.9(1)	30.5(4)	−3.1(1)
	Δ-(λλλ)-*bc*	−4.3(3)	1.2(4)	−119(1)	−104(2)	−5.5(5)	−15(2)	−1.1(5)

[a] Obtained from analyses of $k_q^{\sigma}(T)$ data measured over the 273–308 K temperature range.
[b] Defined according to Eq. (22).
[c] $\Delta\Delta H^{\#} = \Delta H_{\Lambda}^{\#} - \Delta H_{\Delta}^{\#}$; $\Delta\Delta S^{\#} = \Delta S_{\Lambda}^{\#} - \Delta S_{\Delta}^{\#}$; $\Delta\Delta G^{\#} = \Delta\Delta H^{\#} - T\Delta\Delta S^{\#}$.

Table 4
Thermal activation parameters determined for Λ-Tb* and Δ-Tb* quenching processes in H_2O and D_2O solution samples[a]

Solvent	Quencher	$\Delta H^{\#}_{\sigma}$ (kJ mol^{-1})[b]		$\Delta S^{\#}_{\sigma}$ (J mol^{-1} K^{-1})[b]		Enantiodifferential activation parameters[c]		
		Λ-Tb*	Δ-Tb*	Λ-Tb*	Δ-Tb*	$\Delta\Delta H^{\#}$ (kJ mol^{-1})	$\Delta\Delta S^{\#}$ (J mol^{-1} K^{-1})	$\Delta\Delta G^{\#}$ (kJ mol^{-1}) at 293 K
H_2O	Δ-(δδδ)	−3.0(4)	−0.6(1)	−126(2)	−102.9(3)	−2.4(4)	−23(2)	4.3(4)
	Δ-(λδδ)	3.8(4)	2.8(1)	−89(1)	−82.2(4)	1.0(4)	−7(1)	3.1(4)
	Δ-(λλδ)	6.0(3)	−0.2(3)	−76(1)	−96(1)	6.2(4)	20(1)	0.3(4)
	Δ-(λλλ)	5.30(7)	−0.4(2)	−71.6(2)	−100.2(7)	5.7(2)	28.6(7)	−2.7(3)
	Δ-(λλλ)-*mc*	3.93(6)	0.6(2)	−78.0(2)	−97.9(6)	3.3(2)	19.9(6)	−2.5(2)
	Δ-(λλλ)-*bc*	−1.8(2)	2.3(3)	−101(1)	−91(1)	−4.1(3)	−10(1)	−1.1(3)
D_2O	Δ-(δδδ)	−2.7(8)	3.6(2)	−127(3)	−93.1(6)	−6.3(8)	−34(2)	3.7(8)
	Δ-(λδδ)	3.4(3)	2.9(1)	−90(1)	−80.3(2)	0.5(3)	−10(1)	3.4(3)
	Δ-(λλδ)	6.2(2)	0.9(1)	−74.4(4)	−90.4(4)	5.3(2)	16.0(8)	0.6(2)
	Δ-(λλλ)	6.24(5)	−0.5(1)	−67.1(2)	−99.3(5)	6.7(1)	32.2(5)	−2.7(1)
	Δ-(λλλ)-*mc*	5.00(7)	0.2(2)	−74.1(2)	−99.3(7)	4.8(2)	25.2(7)	−2.6(2)
	Δ-(λλλ)-*bc*	−0.83(8)	2.9(1)	−100.0(3)	−91.2(5)	−3.7(2)	−8.8 (8)	−1.1(2)

[a] Obtained from analyses of $k^{\sigma}_{q}(T)$ data measured over the 273–308 K temperature range.
[b] Defined according to Eq. (22).
[c] $\Delta\Delta H^{\#} = \Delta H^{\#}_{\Lambda} - \Delta H^{\#}_{\Delta}$; $\Delta\Delta S^{\#} = \Delta S^{\#}_{\Lambda} - \Delta S^{\#}_{\Delta}$; $\Delta\Delta G^{\#} = \Delta\Delta H^{\#} - T\Delta\Delta S^{\#}$.

the following expression for the ΛL* and ΔL* quenching constants:

$$k^{\sigma}_{q} = \frac{K^{\sigma}_{a} k^{\sigma}_{e}}{1 + \left(k^{\sigma}{}_{-e}/k^{\sigma}_{x}\right) + \left(k^{\sigma}_{e}/k^{\sigma}_{d}\right)}, \tag{26}$$

where $\sigma = \Lambda$ or Δ, and $K^{\sigma}_{a} = k^{\sigma}_{a}/k^{\sigma}_{d}$.

For each of the systems examined in this study, it is expected that $k^{\sigma}_{x} \gg k^{\sigma}{}_{-e}$, in which case Eq. (26) may be reduced to

$$k^{\sigma}_{q} = \frac{K^{\sigma}_{a} k^{\sigma}_{e}}{1 + \left(k^{\sigma}_{e}/k^{\sigma}_{d}\right)}, \tag{27}$$

and this equation may be reformulated to obtain

$$k^{\sigma}_{q} = \left(1 - \frac{k^{\sigma}_{q}}{k^{\sigma}_{a}}\right) K^{\sigma}_{a} k^{\sigma}_{e} \tag{28}$$

In our mechanistic kinetics scheme, k^{Λ}_{a} and k^{Δ}_{a} denote rate constants for the *diffusional association* processes, $\Lambda L^{*} + CQ \rightarrow (\Lambda L^{*} - CQ)$ and $\Delta L^{*} + CQ \rightarrow (\Delta L^{*} - CQ)$, respectively. Calculations of these k^{σ}_{a} rate parameters, using a model based on the Debye–Smoluchowski treatment of the diffusion of charged particles in aqueous solution [31,32], yield k^{σ}_{a} values $> 5 \times 10^{9}$ M^{-1} s^{-1} under all of the conditions represented in our experiments. At any given temperature between 273 and 308 K, the values of k^{σ}_{a} are calculated to be approximately two orders-of-magnitude larger than the largest observed values of the k^{σ}_{q} quenching parameters. These results suggest $k^{\sigma}_{q}/k^{\sigma}_{a}$ ratios sufficiently small to permit the reduction of Eq. (28) to

$$k^{\sigma}_{q} = K^{\sigma}_{a} k^{\sigma}_{e}, \tag{29}$$

which upon comparison with Eq. (27) implies $k^{\sigma}_{e}/k^{\sigma}_{d}$ ratios with values $\ll 1$.

Under the conditions for which Eq. (29) is valid, the K^{Λ}_{a} and K^{Δ}_{a} parameters may be considered quasi-thermodynamic equilibrium constants that reflect the formation and dissociation properties (and thermodynamic 'stabilities') of the (ΛL^{*}–CQ) and (ΔL^{*}–CQ) species formed by diffusional encounters between the luminophore and quencher molecules in solution. The k^{Λ}_{e} and k^{Δ}_{e} parameters are unimolecular rate constants associated with the L*-to-CQ electronic energy-transfer processes that occur *within* the (ΛL^{*}–CQ) and (ΔL^{*}–CQ) encounter complexes.

Based on expressions of k^{Λ}_{q} and k^{Δ}_{q} according to Eq. (29), the enantiodifferential quenching rate

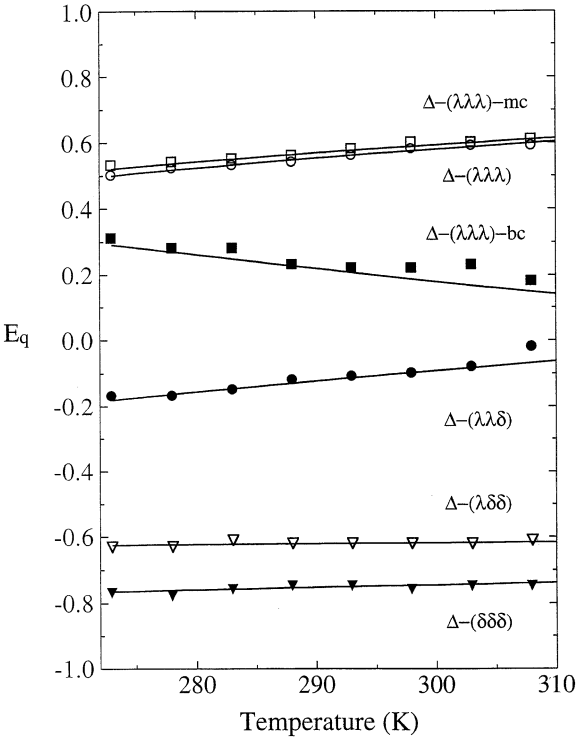

Fig. 12. Plots of $E_q(T)$ data obtained over the 273–308 K temperature range for aqueous (H_2O) solution samples that contained a 10 mM concentration of $Eu(dpa)_3^{3-}$ and a 10 μM concentration of quenchers species. The solid lines shown in the figure represent plots of Eq. (23).

parameter (k_{dq}) may now be written as

$$k_{dq} = k_q^{\Lambda} - k_q^{\Delta} = (1/2)(K_a^{\Lambda} - K_a^{\Delta})(k_e^{\Lambda} + k_e^{\Delta}) + (1/2)(K_a^{\Lambda} + K_a^{\Delta})(k_e^{\Lambda} - k_e^{\Delta}), \quad (30)$$

where the first term on the right-hand side of this equation reflects chiral discriminations in the formation and/or dissociation properties of the (L*–CQ) species, and the second term reflects chiral discriminations in the L*-to-CQ electronic energy-transfer processes. The corresponding expression for the enantioselectivity quenching parameter (E_q) is

$$E_q = \frac{(K_a^{\Lambda}/K_a^{\Delta}) - (k_e^{\Delta}/k_e^{\Lambda})}{(K_a^{\Lambda}/K_a^{\Delta}) + (k_e^{\Delta}/k_e^{\Lambda})} = \frac{1 - (K_a^{\Delta}k_e^{\Delta}/K_a^{\Lambda}k_e^{\Lambda})}{1 + (K_a^{\Delta}k_e^{\Delta}/K_a^{\Lambda}k_e^{\Lambda})}, \quad (31)$$

For the types of systems examined in this study, where the interacting species of interest are oppositely charged ions, the K_a^{σ} parameters (expressed in units of M^{-1}) may be approximated by [11,25]

$$K_a^{\sigma} = 10^{-24}(4\pi\hat{r}_{\sigma}^3/3)N_A \exp\left[-\hat{U}_{\sigma}/RT\right], \quad (32)$$

where N_A is the Avogadro constant, $\hat{r}_{\sigma}$ is defined as the separation distance (in nm) between the metal centers in a (L*–CQ) encounter complex, and $\hat{U}_{\sigma}$ is the energy (per mole) associated with the formation of (L*–CQ) complexes from free L* and CQ species in solution. Given Eq. (32), the ratio of K_a^{Λ} to K_a^{Δ} may be expressed as

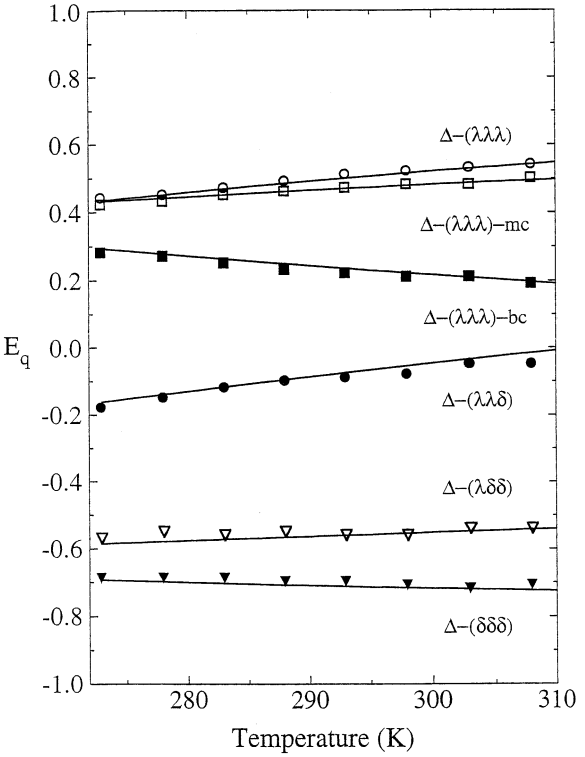

Fig. 13. Plots of $E_q(T)$ data obtained over the 273–308 K temperature range for aqueous (H_2O) solution samples that contained a 10 mM concentration of $Tb(dpa)_3^{3-}$ and a 10 μM concentration of quencher species. The solid lines shown in the figure represent plots of Eq. (23).

$$\frac{K_a^{\Lambda}}{K_a^{\Delta}} = \left(\frac{\hat{r}_{\Lambda}}{\hat{r}_{\Delta}}\right)^3 \exp\left[-\Delta\hat{U}_{cd}/RT\right], \tag{33}$$

where $\Delta\hat{U}_{cd}$ reflects chiral discriminatory contributions to the $\hat{U}_{\sigma}$ interaction energies and is defined as $\Delta\hat{U}_{cd} = \hat{U}_{\Lambda} - \hat{U}_{\Delta}$. If we further define $\hat{r}_m = (\hat{r}_{\Lambda} + \hat{r}_{\Delta})/2$ and $\Delta\hat{r} = \hat{r}_{\Lambda} - \hat{r}_{\Delta}$, and assume $\Delta\hat{r} \ll \hat{r}_m$, then Eq. (33) may be rewritten as

$$\frac{K_a^{\Lambda}}{K_a^{\Delta}} = \exp\left[\frac{3\Delta\hat{r}}{\hat{r}_m} - \frac{\Delta\hat{U}_{cd}}{RT}\right], \tag{34}$$

where $\Delta\hat{r}/\hat{r}_m$ reflects the relative 'compactness' of the (ΛL^*–CQ) vs. (ΔL^*–CQ) complexes (as related to metal–metal separation distances).

Following previous work [11,25], we view energy-transfer processes within the (L*–CQ) encounter complexes as proceeding along a reaction coordinate that passes through a particular nuclear (stereochemical and relative orientational) configuration of the L* and CQ constituents, and express the k_e^{σ} rate constants as

$$k_e^{\sigma} = \kappa_e^{\sigma} \nu_{\sigma}^{\ddagger} \exp\left[-\Delta G_{\sigma}^{\ddagger}/RT\right], \tag{35}$$

where $\Delta G_{\sigma}^{\ddagger}$ represents the free-energy function associated with 'activation' of (L*–CQ) complexes to the critical configuration, $\nu_{\sigma}^{\ddagger}$ denotes the frequency of nuclear motions leading to this configuration, and κ_e^{σ} represents the probability for electronic energy transfer in the activated (L*–CQ)‡ complexes. Given Eq. (35), the ratio of k_e^{Λ} to k_e^{Δ} may be written as

$$\frac{k_e^{\Lambda}}{k_e^{\Delta}} = \frac{\kappa_e^{\Lambda}\nu_{\Lambda}^{\ddagger}}{\kappa_e^{\Delta}\nu_{\Delta}^{\ddagger}} \exp\left[-\Delta G_{cd}^{\ddagger}/RT\right], \tag{36}$$

where

$$\Delta G_{cd}^{\ddagger} = \Delta G_{\Lambda}^{\ddagger} - \Delta G_{\Delta}^{\ddagger}.$$

Substitution of Eqs. (32) and (35) into Eq. (29) gives

$$\begin{aligned} k_q^{\sigma} &= 10^{-24}\left(4\pi\hat{r}_{\sigma}^3/3\right) N_A \kappa_e^{\sigma} \nu_{\sigma}^{\ddagger} \\ &\quad \times \exp\left[-\left(\hat{U}_{\sigma} + \Delta G_{\sigma}^{\ddagger}\right)/RT\right] \\ &\cong 2.523\hat{r}_{\sigma}^3 \kappa_e^{\sigma} \nu_{\sigma}^{\ddagger} \exp\left[-\left(\hat{U}_{\sigma} + \Delta G_{\sigma}^{\ddagger}\right)/RT\right], \end{aligned} \tag{37}$$

and the ratio of k_q^{Λ} to k_q^{Δ} may be written as

$$\begin{aligned} \frac{k_q^{\Lambda}}{k_q^{\Delta}} &= \frac{\kappa_e^{\Lambda}\nu_{\Lambda}^{\ddagger}}{\kappa_e^{\Delta}\nu_{\Delta}^{\ddagger}} \exp\left[3\Delta\hat{r}/\hat{r}_m \right. \\ &\quad \left. - \left(\Delta\hat{U}_{cd} + \Delta G_{cd}^{\ddagger}\right)/RT\right], \end{aligned} \tag{38}$$

If we assume $\nu_{\Lambda}^{\ddagger} = \nu_{\Delta}^{\ddagger} = k_B T/h$, then Eq. (37) may be reformulated to give

$$\begin{aligned} \ln\left(\frac{k_q^{\sigma}}{T}\right) &= \ln\left(\frac{k_B}{h}\right) + \ln\left(2.523\hat{r}_{\sigma}^3 \kappa_e^{\sigma}\right) + \frac{\Delta S_{\sigma}^{\ddagger}}{R} \\ &\quad - \frac{\left(\hat{U}_{\sigma} + \Delta H_{\sigma}^{\ddagger}\right)}{RT}, \end{aligned} \tag{39}$$

and the $\Delta S_{\sigma}^{\#}$ and $\Delta H_{\sigma}^{\#}$ parameters obtained from our fits of the temperature-dependent k_q^{σ} data to Eq. (22) may be expressed as

$$\Delta S_{\sigma}^{\#} = R \ln\left(2.523\hat{r}_{\sigma}^3 \kappa_e^{\sigma}\right) + \Delta S_{\sigma}^{\ddagger}, \tag{40}$$

$$\Delta H_{\sigma}^{\#} = \hat{U}_{\sigma} + \Delta H_{\sigma}^{\ddagger} \tag{41}$$

Furthermore, the enantiodifferential $\Delta\Delta S^{\#}$ and $\Delta\Delta H^{\#}$ parameters may be expressed as

$$\Delta\Delta S^{\#} = R\ln\left(\kappa_e^{\Lambda}/\kappa_e^{\Delta}\right) + 3R\left(\Delta\hat{r}/\hat{r}_m\right) + \Delta S_{cd}^{\ddagger}, \tag{42}$$

$$\Delta\Delta H^{\#} = \Delta\hat{U}_{cd} + \Delta H_{cd}^{\ddagger}, \tag{43}$$

where

$$\Delta S_{cd}^{\ddagger} = \Delta S_{\Lambda}^{\ddagger} - \Delta S_{\Delta}^{\ddagger}$$

and

$$\Delta H_{cd}^{\ddagger} = \Delta H_{\Lambda}^{\ddagger} - \Delta H_{\Delta}^{\ddagger}.$$

For the triply-charged luminophore and quencher systems used in this study it is reasonable to

assume that electrostatic *charge–charge* interactions will make the overwhelmingly dominant contributions to the $\hat{U}_\sigma$ energy functions, in which case these functions may be expressed, to a good approximation, as

$$\hat{U}_\sigma = \frac{10^9 Z_L Z_Q e^2}{4\pi\varepsilon_o D\hat{r}_\sigma(1+\beta\hat{r}_\sigma)} = \frac{1.389x10^5 Z_L Z_Q}{D\hat{r}_\sigma(1+\beta\hat{r}_\sigma)} \ (\text{J mol}^{-1}), \quad (44)$$

where e denotes the elementary charge (1.602×10^{-19} C), ε_o is the vacuum permittivity (8.854×10^{-12} $C^2\,J^{-1}\,m^{-1}$), D is the dielectric constant of the sample medium, β is the inverse Debye length parameter (expressed here in reciprocal nm units), and Z_L and Z_Q denote the 'effective' net charges (in units of e) on the luminophore and quencher species, respectively. Given Eq. (44), the chiral discriminatory $\Delta\hat{U}_{cd}$ energy function may be approximated by

$$\Delta\hat{U}_{cd} = \frac{-1.389x10^5 Z_L Z_Q \Delta\hat{r}(1+2\beta\hat{r}_m)}{D\hat{r}_m^2(1+\beta\hat{r}_m)^2} \ (\text{J mol}^{-1}) \quad (45)$$

Substitution of this expression into Eq. (34) yields the following expression for the ratio of K_a^Λ to K_a^Δ:

$$\frac{K_a^\Lambda}{K_a^\Delta} = \exp\left\{\frac{\Delta\hat{r}}{\hat{r}_m}\left[3+\frac{1.671x10^4 Z_L Z_Q(1+2\beta\hat{r}_m)}{DT\hat{r}_m(1+\beta\hat{r}_m)^2}\right]\right\} \quad (46)$$

The ionic strength of all the solution samples examined in the present study was 0.06 M, and the β parameter in each case may be estimated to have a value of $\sim 0.8\ nm^{-1}$. The *net formal charge* on each of the luminophores was $-3e$, and the *net formal charge* on each of the quenchers was $+3e$. However, results obtained from a previous study [11], in which the ionic-strength dependence of excited-state quenching rates was determined, indicate that for the luminophore–quencher systems examined here the 'effective' charge-product quantity $Z_L Z_Q$ has a value of ~ -4 (rather than the -9 value predicted from the net formal charges on the luminophores and quenchers). If we set $\beta = 0.8\ nm^{-1}$ and $Z_L Z_Q = -4$, assume $D = 81\pm6$ (over the 273–308 K temperature range of our experiments), and assign values of 0.8 ± 0.2 nm to the $\hat{r}_\sigma$ distance parameters, then the values of $\hat{U}_\sigma$ may be estimated to fall within the -3.5 to -8.5 kJ mol^{-1} range, and the values of K_a^σ may be estimated to fall within the 10–20-M^{-1} range. If we further assume $\Delta\hat{r} = \pm0.1\hat{r}_m$ and assign values of 0.8 ± 0.2 nm to $\hat{r}_m$, then the $\Delta\hat{U}_{cd}$ functions may be estimated to have values within the $+1.1$ to -1.1-kJ mol^{-1} range, and the K_a^Λ/K_a^Δ ratios are expected to fall within the 0.85–1.15-range.

Although the electrostatic charge($Z_L e$)–charge($Z_Q e$) interactions considered above are expected to make the most important contributions to the $\hat{U}_\sigma$ and $\Delta\hat{U}_{cd}$ energy functions, other, shorter-range interactions may be expected to play a dominant role in the activation energetics related to $\Delta G_\sigma^\ddagger$ and $\Delta G_{cd}^\ddagger$. These energetics are associated with the relative motions of the luminophore and quencher structures *within* the (L*–CQ) complexes, and it is expected that they will reflect highly anisotropic interactions that have a strong, chirality-related *orientational* dependence, as well as a dependence on the $\hat{r}_\sigma$ contact distance parameters. The interactions that contribute to the κ_e^σ electronic parameters may also be anisotropic, but for the Ln*(donor)–Co(acceptor) systems examined in this study, these interactions most likely reflect a two-electron exchange mechanism in which the κ_e^σ parameters may be presumed to scale (isotropically) with $\exp[-\alpha\hat{r}_\sigma]$, where α is a parameter defined to be identical for $\sigma = \Lambda$ and Δ.

7.2. Eu*–CQ vs. Tb*–CQ quenching

The $Eu(dpa)_3^{3-}$ and $Tb(dpa)_3^3$ luminophores are essentially identical with respect to size, shape, stereochemical details, and distributions of charge, and it is reasonable to assume that the association constants (K_a^σ) of (Eu*–CQ) encounter complexes will be essentially identical to those of the corresponding (Tb*–CQ) complexes. However, the electronic energy-level structures, optical emission

spectra, and excited-state lifetimes of $Eu(dpa)_3^{3-}$ and $Tb(dpa)_3^{3}$ are distinctly different, and one may anticipate differences between the rate constants (k_e^σ) for Ln*-to-Co electronic energy-transfer processes in (Eu*–CQ) vs. (Tb*–CQ) complexes. The $^7F_J \leftarrow {}^5D_4$ emission manifolds of Tb* carry more oscillator strength, span a broader wavelength range, and show greater spectral overlap with Co(III) absorptive transitions than do the $^7F_J \leftarrow {}^5D_0$ emission manifolds of Eu*, but the $4f^6$ electronic configuration of Eu* is expected to have a slightly greater spatial (radial) extent than the $4f^8$ electronic configuration of Tb*. In all of the Eu*–CQ systems examined in this study, it is almost certain that an electron-exchange interaction mechanism will make the dominant contributions to the Eu*-to-Co energy transfer processes. In the Tb*–CQ systems, however, it is possible that both multipole–multipole *and* electron-exchange interaction mechanisms make significant contributions to the Tb*-to-Co energy-transfer processes.

The results obtained in this study show some differentiation between Eu*–CQ and Tb*–CQ quenching kinetics, but the differentiation is relatively weak compared to that related to quencher structure. Under nearly all of the temperature and solvent conditions represented in our experiments, the rate constants determined for σ-Tb* quenching are larger than those determined for σ-Eu* quenching, but in all cases the $k_q^\sigma(Tb^*)/k_q^\sigma(Eu^*)$ ratios are observed to be <2.1. Among the six quencher systems examined in this study, the *bi-capped* Δ-(λλλ)-$[Co(R,R\text{-dach})_3]^{3+}$ complex gives results showing the largest $k_q^\sigma(Tb^*)/k_q^\sigma(Eu^*)$ ratios. The $[CoN_6]^{3+}$ coordination core (and energy-acceptor moiety) of this complex is less accessible to luminophore contact interactions than are those of the other quencher systems, and this most likely diminishes the relative contributions of electron-exchange (vs. multipole–multipole) interactions to the Ln*-to-Co energy-transfer processes. The smallest $k_q^\sigma(Tb^*)/k_q^\sigma(Eu^*)$ ratios are observed in the results obtained for Δ-Ln* quenching by the Δ-(δδδ) and Δ-(λδδ) quencher systems.

The $k_q^\sigma(Tb^*)/k_q^\sigma(Eu^*)$ ratios determined from results obtained on H_2O solution samples (at 293 K) are shown in Table 5. Also shown in Table 5 are comparisons of the k_q^Δ/k_q^Λ and the $k_q^\sigma/2k_q^m$ ratios determined for Eu* and Tb* quenching in H_2O solution samples at 293 K. The $k_q^\sigma/2k_q^m$ ($\sigma \equiv \Lambda$ or Δ) ratio corresponds to the fractional contribution of σ-Ln* quenching to the total (Λ-Ln* plus Δ-Ln*) quenching rate. The k_q^Δ/k_q^Λ and $k_q^\sigma/2k_q^m$ ratios provide alternative measures of the degree and sense of enantioselectivity in the quenching processes, and they are related to the enantioselectivity parameter E_q according to:

$$E_q = \frac{1-\left(k_q^\Delta/k_q^\Lambda\right)}{1+\left(k_q^\Delta/k_q^\Lambda\right)} = \frac{k_q^\Lambda}{2k_q^m} - \frac{k_q^\Delta}{2k_q^m}. \quad (47)$$

The quencher-dependent trends in the k_q^Δ/k_q^Λ, $k_q^\sigma/2k_q^m$, and E_q data are essentially identical for Eu* and Tb*, but the degree of enantioselectivity observed in the Eu* quenching kinetics is on average approximately 10% greater than that observed in the Tb* quenching kinetics. The least differentiation between the Eu* vs. Tb* quenching enantioselectivities is found in the results obtained with the Δ-(λλλ)-*bc* quencher system.

Table 5
Comparisons of the $k_q^\sigma(Tb^*)/k_q^\sigma(Eu^*)$, k_q^Δ/k_q^Λ, and $k_q^\sigma/2k_q^m$ ratios determined for quenching processes in H_2O solution samples at 293 K[a,b]

Quencher	$k_q^\sigma(Tb^*)/k_q^\sigma(Eu^*)$		k_q^Δ/k_q^Λ		$k_q^\Lambda/2k_q^m$		$k_q^\Delta/2k_q^m$	
	Λ	Δ	Eu*	Tb*	Eu*	Tb*	Eu*	Tb*
Δ-(δδδ)	1.27	1.01	7.15	5.71	0.12	0.15	0.88	0.85
Δ-(λδδ)	1.26	1.02	4.32	3.50	0.19	0.22	0.81	0.78
Δ-(λλδ)	l.20	1.13	1.26	1.19	0.44	0.46	0.56	0.54
Δ-(λλλ)	1.11	1.29	0.28	0.33	0.78	0.75	0.22	0.25
Δ-(λλλ)-*mc*	1.22	1.67	0.26	0.36	0.79	0.74	.21	0.26
Δ-(λλλ)-*bc*	2.04	2.03	0.64	0.64	0.61	0.61	0.39	0.39

[a] All data are from measurements performed on solution samples in which the $Eu(dpa)_3^{3-}$ or $Tb(dpa)_3^{3-}$ luminophore concentration was 10 mM and the quencher concentration was 10 μM.

[b] The quenching constants $k_q^\sigma(\sigma \equiv \Lambda$ or $\Delta)$ are defined according to the expressions given in Section 4, and $k_q^m = (k_q^\Lambda + k_q^\Delta)/2$.

7.3. Dependence of quenching rates and enantioselectivities on the details of quencher structure

All of the Co(III) complexes used as quenchers in this study have essentially identical electronic

state structures and excitation properties in the energy regions relevant to Eu*-to-Co and Tb*-to-Co electronic energy-transfer processes. Therefore, one expects very little differentiation among these complexes with respect to satisfying the donor–acceptor level resonance conditions for energy transfer. Moreover, all of the quenchers carry a net charge of $+3e$ and are similar in size, which suggests that the encounter complexes they form with the luminophores in solution will have similar stabilities with respect to electrostatic charge–charge interaction energies. The principal differences between the six quencher complexes are found in the structural details of their constituent ligands and chelate ring systems, and our quenching results show that the relative quenching efficiencies and enantioselectivities exhibited by the six complexes are extraordinarily sensitive to these structural details. It is likely that these structural details have their strongest influence in the energy-transfer step of the overall quenching kinetics, where they modulate the donor–acceptor separation distances and orientational distributions that regulate the k_e^σ rate constants. However, they may also influence the formation properties and stabilities of the luminophore–quencher encounter complexes that are *precursors* to the energy-transfer step. The latter type of influence would be reflected in the K_a^σ (association constant) parameters of the $k_q^\sigma = K_a^\sigma k_e^\sigma$ expressions for the enantiospecific quenching constants.

Each of the four Δ-[Co(*R,R*-dach)$_{3-y}$(*S,S*-dach)$_y$]$^{3+}$ ($y=0$, 1, 2, 3) complexes used as quenchers in this study contains three chelate rings that together form a three-bladed propeller-like structure of *right-handed* screw sense (or helicity) about either an exact or an approximate threefold symmetry axis. However, the four complexes differ with respect to structural details that reflect the absolute stereochemistry of their constituent *R,R*- and/or *S,S*-dach ligands, the conformational properties of the chelate rings (or propeller blades) formed by these ligands, and the orientational distributions of the amino (donor group) N–H bonds that protrude from the two trigonal faces of each complex. The N–H bond orientations are dictated by chelate ring conformational structure, which in turn is dictated by ligand stereochemistry. Both the *R,R*- and *S,S*-dach ligands form rigid, non-planar chelate rings of well-defined symmetry (C_2) and conformational structure, but the *R,R*-dach chelate rings have a conformational chirality (λ opposite that (δ of the *S,S*-dach chelate rings. In our abbreviated notation for the Δ-[Co(*R,R*-dach)$_{3-y}$(*S,S*-dach)$_y$]$^{3+}$ series of complexes, where the $y=0$, 1, 2 and 3 members of the series are denoted by Δ-(λλλ), Δ-(λλδ), Δ-(λδδ) and Δ-(δδδ), respectively, the complexes are distinguished entirely in terms of their distributions of chelate-ring conformational chirality.

The Δ-(λλλ), Δ-(λλδ), Δ-(λδδ) and Δ-(δδδ) quencher structures differ significantly with respect to the orientational distributions of the six N–H (amino group) bonds that protrude from each of their two trigonal faces. These N–H bond orientational distributions are likely to have a significant influence on the relative strengths and geometries of the H-bonding interactions between the amino groups of the quenchers and the carboxylate groups of the Ln(dpa)$_3^{3-}$ luminophore structures, and thus they may be expected to play a significant role in determining the relative stabilities of the various structural configurations within luminophore–quencher encounter complexes. Each trigonal face of the Δ-(λλλ) quencher structure has three N–H bonds that are directed sharply away from the threefold symmetry axis of the structure, and three N–H bonds that are oriented nearly *parallel* to this axis. The latter provide a particularly favorable three-point interaction template for H-bonding with luminophore carboxylate groups. In contrast, all six of the N–H bonds on each trigonal face of the Δ-(δδδ) quencher structure are oriented more or less *obliquely* to the threefold symmetry axis of the structure, and they provide a somewhat less favorable template for H-bonding interactions with the luminophore carboxylate groups. The trigonal faces of the Δ-(λλδ) and Δ-(λδδ) quencher structures have mixtures of N–H bond orientations (parallel to, away from, and oblique to the psuedo C_3 symmetry axis of these structures). In Δ-(λλδ), only two N–H bonds (per trigonal face) are oriented parallel to the psuedo C_3 axis, and in Δ-(λδδ) only one is so oriented.

From the above discussion it may be predicted that for H-bonding interactions at their trigonal

faces, the relative H-bonding capabilities of the Δ-(λλλ), Δ-(λλδ), Δ-(λδδ) and Δ-(δδδ) quenchers will fall in the order Δ-(λλλ) > Δ-(λλδ) > Δ-(λδδ) > Δ-(δδδ). This order is the same as that observed in the quencher dependent trends of the k_q^{Λ} and ε_q^{Δ} results obtained for both Λ-Eu* and Λ-Tb* quenching, and it is the same as that observed in the quencher dependent trends of $k_q^{\Lambda}/k_q^{\Delta}$ ratios measured in the Eu* and Tb* quenching experiments. However, it differs from the order of quencher effectiveness found in the k_q^{Λ} and k_q^{Δ} results, where for both the Δ-Eu* and Δ-Tb* quenching, the order is Δ-(λδδ) > Δ-(λλδ) > Δ-(λλλ) > Δ-(δδδ). These results suggest that luminophore–quencher H-bonding interactions may play a significant role in determining the rates and efficiencies of the Λ-Ln* quenching processes, and that they may also be important in determining the *relative* efficiencies of the Λ-Ln* vs. Δ-Ln* quenching processes.

Comparisons between the results obtained for the Δ-(λλλ), Δ-(λλλ)-*mc* and Δ-(λλλ)-*bc* quenchers give further evidence that quencher N–H bonds may play an important role in regulating the kinetics of Λ-Ln* quenching and in determining the relative rates of Λ-Ln* vs. Δ-Ln* quenching processes. Recall that the structures of Δ-(λλλ)-*mc* and Δ-(λλλ)-*bc* are identical to that of Δ-(λλλ), *except* that in the Δ-(λλλ)-*mc* structure one of the trigonal faces is capped by a tris(methylene)amino group, which eliminates all three axially oriented N–H bonds on that face, and in Δ-(λλλ)-*bc* both trigonal faces are capped by tris(methylene)amino groups, which eliminate all the axially oriented N–H bonds on the two trigonal faces of the quencher structure. The relative efficiencies of Δ-(λλλ), Δ-(λλλ)-*mc* and Δ-(λλλ)-*bc* as quenchers of Λ-Eu* and Λ-Tb* fall in the order Δ-(λλλ) > Δ-(λλλ)-*mc* > Δ-(λλλ)-*bc*. Expressed as ratios, the relative efficiencies are 1.84:1.63:1 for Λ-Eu* quenching in H_2O solutions, and 1.23:1.16:1 for Λ-Tb* quenching in H_2O solutions. There is considerably less differentiation between Δ-(λλλ), Δ-(λλλ)-*mc* and Δ-(λλλ)-*bc* in their quenching of Δ-Eu* and Δ-Tb* (see the results given in Table 2). The enantioselectivies (E_q-values) exhibited by Δ-(λλλ)-*mc* are very similar to those exhibited by Δ-(λλλ), but those exhibited by Δ-(λλλ)-*bc* are more than a factor of two smaller in magnitude. This suggests that chiral discrimination in the quenching processes are dependent to at least some extent on luminophore access to (or docking at) an open, non-capped trigonal face of a quencher molecule, where N–H bonds are available and favorably oriented for H-bonding interactions with the luminophore carboxylate groups.

The most striking results obtained in this study are those reflected in the relative signs and magnitudes of the E_q enantioselectivity parameters (and the $\Delta\Delta G^{\#}$ enantiodifferential activation parameters) determined for the Δ-(λλλ), Δ-(λλδ), Δ-(λδδ) and Δ-(δδδ) series of quenchers. In both H_2O and D_2O solution samples, at all temperatures between 273 and 308 K, the Δ-(λλλ) quencher exhibits a preference for Λ-Ln* over Δ-Ln* quenching ($E_q > 0$ and $\Delta\Delta G^{\#} < 0$), whereas each of the Δ-(λλδ), Δ-(λδδ) and Δ-(δδδ) quenchers exhibit a preference for Λ-Ln* over Δ-Ln* quenching ($E_q < 0$ and $\Delta\Delta G^{\#} > 0$), with Δ-(λλδ) showing the weakest enantioselectivity in its quenching actions and Δ-(δδδ) showing the strongest (see relevant data in Table 2 and in Figs. 12 and 13). These results show that replacement of just one of the *R,R*-dach ligands in Δ-(λλλ)-$[Co(R,R\text{-dach})_3]^{3+}$ with an *S,S*-dach ligand, to form Δ-(λλδ)-$[Co(R,R\text{-dach})_2(S,S\text{-dach})]^{3+}$, is sufficient to change the enantiopreferences in the Λ, Δ-Ln* quenching processes from a Λ-Ln* preference to a Δ-Ln* preference. It is clear that both the degree and sense of the chiral discriminations evident in the luminophore–quencher interaction processes are governed predominantly by the structural chirality present in the individual chelate rings of the Δ-$[Co(R,R\text{-dach})_{3-y}(S,S\text{-dach})_y]^{3+}$ complexes, rather than by the overall configurational chirality (Δ) of these complexes. Structural details in the individual propeller blades (chelate rings) of these three-bladed propeller-like systems play a more important role in differentiating between the Λ-Ln* and Δ-Ln* luminophores than does the screw sense of the overall propeller structure. Incremental structural changes in the individual propeller blades of these systems lead to pronounced changes in their chiral recognition/discrimination behavior.

7.4. Temperature dependence of quenching rates and enantioselectivity

The temperature dependence of the k_q^σ rate-constant data is well represented by either Arrhenius or Eyring type plots (based on Eqs. (21) and (22), respectively), and the temperature dependence of the E_q (enantioselectivity parameter) data is well represented by the expression for E_q given in Eq. (23). Eyring type plots of the $k_q^\sigma(T)$ data are shown in Figs. 9–11, and E_q vs. T plots are shown in Figs. 12 and 13. The $\Delta H_\sigma^\#$, $\Delta S_\sigma^\#$, $\Delta\Delta H^\#$, $\Delta\Delta S^\#$ and $\Delta\Delta G^\#$ parameter values obtained from the Eyring type analyses are presented in Tables 3 and 4.

According to the mechanistic considerations presented in Section 7.1, the temperature dependence of the quenching constants k_q^σ will reflect (a) the temperature-dependent properties of the luminophore (L*)–quencher(CQ) association/dissociation processes, $L^* + CQ \leftrightarrows (L^* - CQ)$ and (b) the thermal requirements for structural reorganizational motions that facilitate $(L^* - CQ) \rightarrow (L - CQ^*)$ electronic energy-transfer processes *within* the (L*–CQ) encounter complexes. For all of the systems examined in the present study the (L*–CQ) complexes are formed from oppositely charged molecular ions, and one may expect their formation energetics to make substantial *exothermic* contributions to the phenomenological $\Delta H_\sigma^\#$ parameters derived from our Eyring-type analyses of the $k_q^\sigma(T)$ data. In Section 7.1 we estimated that the values of these contributions (denoted by $\hat{U}_\sigma$ in Eq. (41)) should be in the -3.5 to -8.5-kJ mol^{-1} range, and that the association constants (K_a^σ) of the (L*–CQ) complexes should have values in the 10–20-M^{-1} range. The thermal energy requirements for 'activating' the electronic energy-transfer processes *within* the (L*–CQ) complexes are somewhat more difficult to assess in the absence of any detailed knowledge about the dominant energy-transfer mechanisms and their dependence on the relative motions and orientations of the L* and CQ structures in the (L*–CQ) complexes. It is clear, however, that these requirements will be reflected in $\Delta H_\sigma^\ddagger > 0$ contributions to the $\Delta H_\sigma^\#$ parameters defined by Eq. (41).

It is difficult to make any detailed interpretive comments about the results shown in Tables 3 and 4 without indulging in excessive speculation about the interaction mechanisms operative in the quenching processes. We will not do that here, but modeling studies are underway that may help give detailed interpretations in the future. It is clear that the thermal activation parameters shown in Tables 3 and 4 exhibit significant variations with changes in quencher structure, but these variations across the quencher series differ, both qualitatively and quantitatively, for Λ-Eu* vs. Δ-Eu* and Λ-Tb* vs. Δ-Tb* quenching. The results obtained from measurements on H_2O solution samples are qualitatively similar to those obtained for D_2O solution samples, but there are small quantitative differences between these two sets of results. Perhaps the most striking results are those obtained for Λ- and Δ-Eu* quenching by the Δ-(δδδ) quencher structure (Table 3). This quenching is characterized by large negative values for both the $\Delta H_\sigma^\#$ and $\Delta S_\sigma^\#$ parameters, and by $\Delta G_\sigma^\#$ values that vary from 31.5 to 36.4 kJ mol^{-1} for Λ-Eu* quenching and from 26.9 to 31.6 kJ mol^{-1} for Δ-Eu* quenching over the 273–308 K temperature range, in H_2O solution samples. These results may be compared to those obtained for Λ-Eu* and Δ-Eu* quenching by the Δ-(λδδ) quencher structure, which differs from Δ-(δδδ) by the replacement of just one *S*,*S*-dach ligand with a *R*,*R*-dach ligand (Fig. 2). The Λ- and Δ-Eu* quenching by Δ-(λδδ) is characterized by $\Delta H_\sigma^\# > 0$ and $\Delta S_\sigma^\# < 0$ parameter values, and by $\Delta G_\sigma^\#$ values that vary from 28.6 to 31.8 kJ mol^{-1} for Λ-Eu* quenching and from 25.3 to 28.2 kJ mol^{-1} for Δ-Eu* quenching over the 273–308-K temperature range.

Another interesting comparison can be made between the thermal activation parameters obtained for Λ- and Δ-Eu* quenching by the Δ-(λλλ), Δ-(λλλ)-*mc* and Δ-(λλλ)-*bc* quencher structures. In particular, we note that whereas the $\Delta H_\sigma^\#$, $\Delta S_\sigma^\#$, $\Delta\Delta H^\#$ and $\Delta\Delta S^\#$ parameter values determined for Δ-(λλλ) are similar in magnitude and identical in sign to those determined for Δ-(λλλ)-*mc,* the $\Delta H_\sigma^\#$, $\Delta\Delta H^\#$ and $\Delta\Delta S^\#$ parameter values determined for Δ-(λλλ)-*bc* have signs *opposite* those determined for Δ-(λλλ) and Δ-(λλλ)-*mc*. Additionally, we note from the E_q vs. T data plots shown in Figs. 12 and 13 that the enantioselectivity

of Δ-(λλλ)-*bc* exhibits a temperature dependence both qualitatively and quantitatively different from that exhibited by Δ-(λλλ) and Δ-(λλλ)-*mc*. The only structural differences between the Δ-(λλλ), Δ-(λλλ)-*mc* and Δ-(λλλ)-*bc* quenchers are found on the trigonal faces of their structures, the details of which were described in Section 7.3.

7.5. Solvent dependence

The unquenched excited-state lifetimes (τ_0) and $\Lambda \leftrightarrows \Delta$ enantiomer interconversion rates of $Eu(dpa)_3^{3-}$ and $Tb(dpa)_3^{3-}$ are different in H_2O vs. D_2O solutions [9–11,23,33]. Over the 273–308-K temperature range, the τ_0 values for Eu* vary from 1.64 to 1.60 ms in H_2O solutions and from 3.19 to 3.11 ms in D_2O. Over this same temperature range, the τ_0 values for Tb* vary from 2.10 to 2.08 ms in H_2O solutions and from 2.24 to 2.22 ms in D_2O. Thus changing from H_2O to D_2O solution samples in our quenching experiments we could lengthen the time period over which luminophore–quencher encounters and quenching actions could occur. Furthermore, since it is known that the $\Lambda \leftrightarrows \Delta$ enantiomer interconversion rates of $Ln(dpa)_3^{3-}$ are different in H_2O vs. D_2O solutions, it is reasonable to assume that any structural changes necessary for promoting electronic energy-transfer processes in the luminophore–quencher encounter complexes might also be solvent (H_2O vs. D_2O) dependent.

As described in Section 4, both the solvent dependence and the temperature dependence of the unquenched excited-state decay constants ($k_0 \equiv 1/\tau_0$) and the enantiomer interconversion rate constants (k_c) are taken into account when our TR-CL data are analyzed to obtain values for the k_q^σ quenching constants (Eqs. (7)–(15), and the associated discussion). Moreover, the k_0 decay constants appear explicitly in our definition of the quenching efficiency parameters ε_q^σ (Eq. (18)).

From the results shown in Table 2, we note that both the quenching constants (k_q^σ) and the quenching efficiency parameters (ε_q^σ) exhibit significant solvent (H_2O vs. D_2O) dependent behavior, whereas the enantioselectivity parameters (E_q) show very little solvent dependence. Among the $\Delta H_\sigma^\#$ and $\Delta S_\sigma^\#$ results shown in Tables 3 and 4, very little solvent dependence is observed in the $\Delta S_\sigma^\#$ data, but for several of the luminophore–quencher systems, the $\Delta H_\sigma^\#$ parameters exhibit a quite significant solvent dependence (see, in particular, the results listed for the Δ-(δδδ) quencher).

8. Conclusion

The results obtained in this work demonstrate the extraordinary sensitivity of intermolecular chiral recognition/discrimination processes to small changes in molecular electronic and stereochemical structure. In all of the systems examined here, the interacting chiral molecules have three-bladed propeller-like structures of similar overall shapes and sizes, and in all cases the interaction events occur in transient encounters between the molecules (rather than in long-lived *static* complexes). The systems differ only with respect to either (a) a change in the electronic state structure of one of the interacting molecules (as in replacing Eu* with Tb* luminophores), or (b) small structural changes in one or more of the propeller blades of the other interacting molecule (as in the series of Δ-$[Co(R,R\text{-dach})_{3-y}(S,S\text{-dach})_y]^{3+}$ ($y = 0$, 1, 2 or 3) molecules). It was found that these types of small changes in the structures of the interaction partners can lead to remarkably large changes in the chiral recognition and discrimination properties of the systems.

Several types of intermolecular interaction rate processes contribute to the enantio-differential excited-state quenching kinetics monitored by our TR-CL measurements. These rate processes include (a) those governing the formation/dissociation dynamics (and lifetimes) of the luminophore(L*)–quencher(CQ) encounter complexes in solution, (b) those reflecting structural reorganizational dynamics within the (L*–CQ) complexes, and (c) those governing the rates of electronic energy-transfer, $(L^* - CQ) \rightarrow (L - CQ^*)$, events within the encounter complexes. For the systems examined in this study, it is expected that the processes referred to in (b) will be most sensitive to the stereochemical details of the interacting L* and CQ molecules and will make the dominant contributions to the chiral discriminations observed

in the enantiodifferential, ΛL^* vs. ΔL^*, quenching kinetics measured in our TR-CL experiments.

The enantioselectivity results obtained in this study show that small changes in the stereochemical structures of the CQ molecules can produce changes in both the sign and magnitude of the enantioselectivity parameter (E_q). However, for any given CQ structure, the E_q parameter values obtained for Eu* quenching are very similar to those obtained for Tb* quenching. The $Eu(dpa)_3^{3-}$ and $Tb(dpa)_3^{3-}$ complexes used as luminophores in the present study differ somewhat in the details of their electronic energy-level structures and excited-state decay properties; but in each case the excitation and deexicitation processes relevant to their use in our experiments involve intraconfigurational 4f–4f electronic transitions which are relatively insensitive to any structural changes that occur outside the inner-coordination sphere of the lanthanide ion. This, combined with the fact that the stereochemical structures of the Λ- and Δ-$Eu(dpa)_3^{3-}$ complexes are essentially identical to those of the Λ- and Δ-$Tb(dpa)_3^{3-}$ complexes, can explain in large part why the enantioselectivities observed in our Eu* and Tb* quenching experiments are very similar.

For all of the systems examined in this study, the excited-state quenching rates are observed to be at least two orders-of-magnitude slower than the rates of diffusional encounters between the luminophore and quencher species (in both H_2O and D_2O solutions), and the time periods over which quenching actions can occur are determined by the unquenched excited-state lifetimes of the Eu* and Tb* luminophores. The observational time periods used in making our TR-CL measurements were generally of 6–8 ms duration, sufficient in all cases for monitoring at least 90% of the luminescence intensity decay. Over these time periods, it is possible for a quencher molecule to have multiple collisional encounters with excited luminophores and participate in multiple quenching events. This accounts, in part, for our observation that only a small concentration of quencher molecules in our solution samples is needed to generate a large enantiomeric excess in the luminophore excited-state population within the 6–8-ms observational time periods. Attention is drawn to the results shown in Fig. 8, which were obtained on aqueous (H_2O) solution samples that contained a 10 mM concentration of $Eu(dpa)_3^{3-}$ and a 10 μM concentration of quencher molecules. Those results show the time development of enantiomeric excess produced in the Eu* excited-state population by the enantiopreferential quenching actions of the various quencher molecules used in this study. Note that three of the quenchers produce enantiomeric excess values >0.7 (in magnitude) within 3 ms after the Eu* excited-state population is prepared (in a racemic state, via excitation with linearly polarized laser light at 465.8 nm).

The results shown in Fig. 8 were obtained under conditions in which the time-dependent enantiomeric excess function $\eta_{em}(t)$, defined earlier in Eq. (20), may be reduced to the form $\eta_{em}(t) = \tanh(-k_{dq}[CQ]t/2)$, where $k_{dq} = k_q^{\Lambda} - k_q^{\Delta}$. Comparing the data shown in Table 2 for the various quencher molecules, we note that although the Δ-(δδδ) quencher exhibits a greater enantioselectivity, $|E_q|$, than any of the other quenchers, its $|k_{dq}|$ values are smaller than those determined for the Δ-(λδδ), Δ-(λλλ) and Δ-(λλλ)-*mc* quenchers. This is reflected in the $\eta_{em}(t)$ results obtained for Eu* quenching, as shown in Fig. 8, and also in the analogous results obtained for Tb* quenching [30].

Acknowledgments

This work was supported by grants from the US National Science Foundation and the University of Virginia Pratt Endowment Fund. The basic ideas for this work originated with the senior author (F.S.R.) while he was a graduate student in Prof. Walter Kauzmann's laboratory at Princeton University. It was then that he learned about molecular chirality and optical activity from Prof. Kauzmann and became fascinated with the theory and measurement of chirality-dependent phenomena. F.S.R. wishes to express his profound gratitude and deep appreciation to Prof. Kauzmann for his rigorous (and patient) mentorship, his example of absolute integrity in personal and professional conduct, and his enormous generosity in sharing his knowledge and philosophical ruminations. Prof. Kauzmann's influence as a teacher and scientist has a reach

and a longevity that extend far beyond any normal bounds.

References

[1] D.P. Craig, D.P. Mellor, Topics Curr. Chem. 63 (1976) 1.
[2] D.P. Craig, in: S.F. Mason (Ed.), Optical Activity and Chiral Discrimination, Reidel, Dordrecht, 1979, pp. 293–318.
[3] S.F. Mason, in: S.F. Mason (Ed.), Optical Activity and Chiral Discrimination, Reidel, Dordrecht, 1979, pp. 319–337.
[4] S.F. Mason, Molecular Optical Activity and Chiral Discriminations, Cambridge University Press, Cambridge, 1982.
[5] D.P. Craig, T. Thirunamachandran, Molecular Quantum Electrodynamics, Academic Press, New York, 1984, pp. 142–182, Chapter 7.
[6] L. Salem, X. Chapuisat, G. Segal, et al., J. Am. Chem. Soc. 109 (1987) 2887.
[7] D.H. Metcalf, S.W. Snyder, J.N. Demas, F.S. Richardson, J. Am. Chem. Soc. 112 (1990) 5681–5695.
[8] D.H. Metcalf, J.M.McD. Stewart, S.W. Snyder, C.M. Grisham, F.S. Richardson, Inorg. Chem. 31 (1992) 2445–2455.
[9] D.H. Metcalf, J.P. Bolender, M.S. Driver, F.S. Richardson, J. Phys. Chem. 97 (1993) 553–564.
[10] J.P. Bolender, D.H. Metcalf, F.S. Richardson, Chem. Phys. Lett. 213 (1993) 131.
[11] D.P. Glover-Fischer, D.H. Metcalf, J.P. Bolender, F.S. Richardson, Chem. Phys. 198 (1995) 207–234.
[12] T. Gowl Stockman, C.A. Klevickis, C.M. Grisham, F.S. Richardson, J. Mol. Recog. 9 (1996) 595–606.
[13] R.B. Rexwinkle, S.C.J. Meskers, J.P. Riehl, H.P.J.M. Dekkers, J. Phys. Chem. 97 (1993) 13519–13526.
[14] R.B. Rexwinkle, S.C.J. Meskers, J.P. Riehl, H.P.J.M. Dekkers, J. Phys. Chem. 97 (1993) 3875–3884.
[15] R.B. Rexwinkle, S.C.J. Meskers, J.P. Riehl, H.P.J.M. Dekkers, J. Phys. Chem. 96 (1992) 1112–1120.
[16] R.B. Rexwinkle, S.C.J. Meskers, J.P. Riehl, H.P.J.M. Dekkers, J. Phys. Chem. 96 (1992) 5725–5733.
[17] C.L. Maupin, S.C.J. Meskers, H.P.J.M. Dekkers, J.P. Riehl, Chem. Commun. (1996) 2457–2458.
[18] T.A. Hopkins, J.P. Bolender, D.H. Metcalf, F.S. Richardson, Inorg. Chem. 35 (1996) 5347–5355.
[19] T.A. Hopkins, J.P. Bolender, D.H. Metcalf, F.S. Richardson, Inorg. Chem. 35 (1996) 5356–5362.
[20] Y. Saito, Inorganic Molecular Dissymmetry, Springer, Berlin, 1979.
[21] C.J. Hawkins, Absolute Configuration of Metal Complexes, Wiley-Interscience, New York, 1971.
[22] F.S. Richardson, Chem. Rev. 79 (1979) 17–42.
[23] D.P. Glover-Fischer, D.H. Metcalf, T.A. Hopkins, et al., Inorg. Chem. 37 (1998) 3026–3033.
[24] B. Wilson, E.I. Solomon, J. Am. Chem. Soc. 102 (1980) 4085.
[25] F.S. Richardson, D.H. Metcalf, D.P. Glover, J. Phys. Chem. 95 (1991) 6249–6260.
[26] F.S. Richardson, D.H. Metcalf, in: K. Nakanishi, N. Berova, R.W. Woody (Eds.), Circular Dichroism: Principles and Applications, VCH Publishers, New York, 1994, pp. 153–177, chapter 7.
[27] S.E. Harnung, B.S. Sorensen, I. Creaser, H. Maegaard, U. Pfenninger, C.E. Schaffer, Inorg. Chem. 15 (1976) 2123–2126.
[28] I.I. Creaser, J.MacB. Harrowfield, A.J. Herlt, et al., J. Am. Chem. Soc. 99 (1977) 3181–3182.
[29] R.J. Geue, M.G. McCarthy, A.M. Sargesen, J. Am. Chem. Soc. 106 (1984) 8282–8291.
[30] J.P. Bolender, Ph.D. dissertation, University of Virginia, 1994.
[31] C. Chiorboli, M.T. Indelli, M.A.R. Scandola, F. Scandola, J. Phys. Chem. 92 (1988) 156.
[32] D.P. Glover-Fischer, Ph.D. dissertation, University of Virginia, 1994.
[33] D.H. Metcalf, S.W. Snyder, J.N. Demas, F.S. Richardson, J. Am. Chem. Soc. 112 (1990) 469–479.